



Global footprints of dansgaard-oeschger oscillations in a GCM

Kenji Izumi^{a, b, *}, Edward Armstrong^{a, b, c}, Paul Valdes^{a, b}^a School of Geographical Sciences, University of Bristol, UK^b Cabot Institute, University of Bristol, UK^c Department of Geosciences and Geography, University of Helsinki, Finland

ARTICLE INFO

Article history:

Received 31 October 2022

Received in revised form

17 February 2023

Accepted 19 February 2023

Available online 2 March 2023

Handling Editor: A. Voelker

Keywords:

Dansgaard-oeschger oscillations

Palaeoclimate modelling

Climate changes

Vegetation changes

ABSTRACT

The mechanisms driving the Dansgaard-Oeschger (DO) cycles remain uncertain, but promising hypotheses could explain it, and a comprehensive assessment of its impact is needed. We have identified DO-like millennial-scale climate variability in a glacial simulation based on the salt oscillator hypothesis with the HadCM3B-M2.1 coupled atmosphere-ocean-vegetation model. The simulated DO-like warming shows temperature changes of 7.1 ± 2.5 °C in Greenland, comparable to DO9 and DO6, the smallest temperature changes of the observed DO events. This study focuses on the impacts of DO-like events on climate and vegetation beyond the North Atlantic. We find that the simulated warming in the Northern Hemisphere extratropics during Greenland interstadials agree with available proxy estimates. The simulated tropical hydroclimatic responses during the interstadials, such as northward propagation of the Intertropical Convergence Zone, strengthening of some Northern Hemisphere summer monsoons, and weakening of some Southern Hemisphere monsoons, are also consistent with proxy estimates. Moreover, simulated vegetation cover in the Northern Hemisphere increases during interstadials relative to stadials, while no large-scale dominant vegetation changes are consistent with observed biome changes associated with DO6. Our simulation based on the salt oscillator hypothesis can account for many observed features of DO events. However, it cannot simulate several observed climate responses in the equatorial Indian and western Pacific Oceans, including the East Asian and South African monsoon. The causes of those mismatches need to be further explored, whether they are hypothesis-dependent or model-dependent.

© 2023 The Authors. Published by Elsevier Ltd. This is an open access article under the CC BY license (<http://creativecommons.org/licenses/by/4.0/>).

1. Introduction

The oxygen isotope composition ($\delta^{18}\text{O}$) in Greenland ice cores reveals large and rapid millennial-scale variability during the last glacial period (roughly 115,000–10,000 years ago before the present; 115 ka–10 ka BP), reflecting local temperature changes (Dansgaard et al., 1993). These Greenland warmings, commonly referred to as Dansgaard-Oeschger (DO) events, were some of the largest and fastest temperature shifts during the last glacial period. Their amplitude ranges from 5 °C to 16.5 °C, with abrupt warming completed within a few centuries (Kindler et al., 2014). These DO events were followed by a period of warm temperatures (termed interstadials) during which the temperature gradually decreased, followed by an abrupt switch to a stable cold condition (termed stadials). This succession constitutes a DO cycle. DO events have

been estimated to occur approximately every 1500 years (Schulz, 2002), although there is no statistically significant evidence for a clear periodicity (Ditlevsen et al., 2007). DO thermal oscillations were correlated with a shift in North Atlantic sea surface temperature (the Bond cycles; Bond et al., 1993) and with episodes of massive iceberg discharge into the North Atlantic (Heinrich events; HE; Bond et al., 1992).

DO events exhibit clear regional and global impacts in marine and terrestrial data. Several studies have summarised these patterns (Harrison and Sánchez Goñi, 2010; Hemming, 2004; Overpeck and Cole, 2006; Voelker, 2002). During interstadials, warming is not just isolated to the North Atlantic, with many regions over Eurasia and North America also becoming warmer and wetter (Asmerom et al., 2010; Benson et al., 2003; Denniston et al., 2007; Fleitmann et al., 2009; Fletcher and Sánchez Goñi, 2008; Genty et al., 2005; Grygar et al., 2006; Moseley et al., 2014; Nebout et al., 2002; Roucoux et al., 2001, 2005; Rousseau et al., 2007; Sánchez Goñi et al., 2000, 2008; Sinopoli et al., 2018, 2019; Stockhecke et al., 2016; Wagner et al., 2010; Wei et al., 2021).

* Corresponding author. School of Geographical Sciences, University of Bristol, UK.
E-mail address: kenji.izumi@bristol.ac.uk (K. Izumi).

Several monsoons in the Northern Hemisphere (the East Asian, Indian and West African monsoons) strengthened (Corrick et al., 2020; Deplazes et al., 2014; Dong et al., 2018; Duan et al., 2014; Kathayat et al., 2016; Lauterbach et al., 2020; Mingram et al., 2018; Mulitza et al., 2008; Schulz et al., 1998; Schulz, 2002; Wang et al., 2001; Weldeab, 2012; Zorzi et al., 2022). A northward shift of the Intertropical Convergence Zone (ITCZ) caused wetter conditions in the tropical Northern Hemisphere and drier conditions over the tropical Southern Hemisphere (Bayon et al., 2017; Cheng et al., 2013; Deplazes et al., 2013; Kanner et al., 2012; Leduc et al., 2007; Medina-Elizalde et al., 2017; Mosblech et al., 2012; Peterson et al., 2000; Turney et al., 2004; Wang et al., 2004; Ziegler et al., 2013). Antarctica ice cores show cooling, consistent with an increase of northward heat transport from the Southern Hemisphere (Buizert et al., 2015; Wolff et al., 2010). Table 1 summarizes the observed global footprints of the Greenland interstadials.

The mechanisms driving the DO cycles remain uncertain, however, most theories focus on variability in the Atlantic Meridional Overturning Circulation (AMOC) that transports surface/upper-level water masses northward and returns them southward to the deep ocean (Ganopolski and Rahmstorf, 2001; Knutti et al., 2004). A strong AMOC increases northward oceanic heat transport and warms the northern climate and vice versa. This AMOC phase shift can happen abruptly in response to the freshwater balance of the North Atlantic. The relationship between DO cycles and AMOC strength has been inferred from a deep North Atlantic sediment core (Henry et al., 2016), but paleo-oceanographic evidence for AMOC phase shifts by freshwater forcing remains elusive (Petersen et al., 2013; Piotrowski et al., 2008; Pisias et al., 2010). Other mechanisms/hypotheses proposed (e.g., reorganizations of the tropics with the ocean thermohaline circulation in the tropics, changes in wind patterns such as extratropical jets and storm tracks, sea-ice variability and feedbacks, and ice-shelf growth and decay) are comprehensively described in Clement and Peterson (2008) and Li and Born (2019). Each alternate hypothesis can account for some observed features of DO cycles, but the AMOC hypothesis remains central to the discussion because

it captures much of the spatial pattern in climate changes.

Simulating the DO events using a coupled climate model remains challenging. To date only a few models have demonstrated DO scale oscillations when incorporating fully glacial boundary conditions. These are the University of Toronto version of the CCSM4 model (UofT-CCSM4; Peltier et al., 2020; Peltier and Vettoretti, 2014; Vettoretti and Peltier, 2016, 2018), the University of Tokyo MIROC model (MIROC4m; Kuniyoshi et al., 2022), the Max Planck Institute Earth System Model (MPI-ESM; Klockmann et al., 2020), and the University of Bristol version of the HadCM3 model (HadCM3B; Armstrong et al., 2022). All these studies have linked the DO cycles with the salt oscillator hypothesis.

Armstrong et al. (2022) investigate the mechanism of the DO-like cycles in HadCM3B, concluding that regime shifts in the AMOC drive the oscillation in response to build up and collapse of the salinity gradient in the North Atlantic between the subtropical gyre and northern North Atlantic. A full set of model salinity diagnostics shows that a complex ocean-atmosphere-sea-ice feedback mechanism maintains this oscillator and that the extent of the Laurentide ice sheet, which influences large-scale atmospheric and ocean circulation, is the key trigger. Since the salt oscillator hypothesis based on climate and ocean variabilities over the North Atlantic can explain the mechanism driving the DO-like oscillations, a comprehensive assessment of the impact of that DO-like events is required next. Utilising the same climate model set-up and boundary conditions used in Armstrong et al. (2022), this study investigates large-scale variations in the simulated climate and vegetation associated with DO-like unforced millennial-scale oscillations beyond the North Atlantic. It is useful to assess the millennial-scale impact of climate on vegetation distribution during a glacial climate especially using a dynamic vegetation scheme. Finally, we compare the features resulting from the DO-like oscillations based on the salt oscillator hypothesis with available proxy records and summarise which features can be simulated and which cannot.

Table 1

Global impacts of warmer North Atlantic events (interstadials) relative to stadials associated with either Heinrich events (massive North American iceberg discharges) or with episodes of British-Icelandic-Scandinavian iceberg discharges.

Region or system	Response(s)	Reference(s)
Greenland	Abrupt-large warming	Kindler et al., (2014)
Central Europe	Warmer and wetter	Genty et al., (2005); Rousseau et al., (2007); Sánchez Goñi et al., (2000); Sánchez Goñi et al., (2008); Moseley et al., (2014); Wei et al., (2021)
Western Europe/western Mediterranean	Warmer and wetter	Rouxoux et al., (2001); Nebout et al., (2002); Rouxoux et al., (2005); Fletcher and Sánchez Goñi (2008); Sánchez Goñi et al., (2008)
Eastern Mediterranean	Warmer and wetter	Fleitmann et al., (2009); Stockhecke et al., (2016); Sinopoli et al., (2018), 2019
East Central Siberia	Warmer and wetter	Grygar et al., (2006)
The Great Basin	Warmer and wetter	Benson et al., (2003); Denniston et al., (2007)
Southwestern USA	Warmer and drier	Asmerom et al., (2010); Wagner et al., (2010)
The Pacific Northwest	Warmer	Grigg and Whitlock (2002)
The Florida Peninsula	Drier	Grimm et al., (2006)
West African monsoon	Stronger summer monsoon	Mulitza et al., (2008); Weldeab (2012)
East Asian monsoon	Stronger summer monsoon	Wang et al., (2001); Takahara et al., (2010); Duan et al., (2014); Dong et al., (2018); Mingram et al., (2018)
Indian monsoon	Stronger summer monsoon	Schulz et al., (1998); Deplazes et al., (2014); Kathayat et al., (2016); Lauterbach et al., (2020); Zorzi et al., (2022)
Central America/Tropical North Atlantic	Wetter in tropical Americas, ITCZ northward	Peterson et al., (2000); Leduc et al., (2007); Deplazes et al., (2013); Medina-Elizalde et al., (2017); Mosblech et al., (2012)
South American summer monsoon	Weaker summer monsoon	Wang et al., (2004); Kanner et al., (2012); Cheng et al., (2013)
South African monsoon	Weaker summer monsoon	Ziegler et al., (2013)
subtropical Australia	ITCZ equatorward	Bayon et al., (2017)
NW tropical Pacific	Lower salinity	Stott et al. (2002)
NE Australia	Drier	Turney et al., (2004)
Antarctica	Gradual-small cooling	Wolff et al., (2010); Buizert et al., (2015)

2. Model and methodology

2.1. Model description – the HadCM3 earth system model

We use the coupled atmosphere and ocean model HadCM3 (the Hadley Centre Coupled Model version3; [Gordon et al., 2000](#)), in particular, the version HadCM3B-M2.1 reported by [Valdes et al. \(2017\)](#), which includes a thermodynamic and free-drift sea ice model. The model configurations of HadCM3B-M2.1 are similar to those in the original reference ([Gordon et al., 2000](#)) but contain several small bug fixes and model improvements ([Valdes et al., 2017](#)). The atmospheric component is run with 96×73 latitude-longitude grid boxes ($3.75^\circ \times 2.5^\circ$) and 19 levels in the vertical, and the ocean component is run with 288×144 latitude-longitude ($1.25^\circ \times 1.25^\circ$) and 20 vertical levels.

HadCM3B-M2.1 uses MOSES2.1 (Met Office Surface Exchange Scheme version 2.1) land-surface scheme, which calculates the fluxes of water and energy at the Earth's surface-atmosphere interface and incorporates the physiological impact of atmospheric carbon dioxide, water vapour, and temperature on photosynthesis and stomatal conductance ([Cox et al., 2000](#); [Essery et al., 2001](#); [Valdes et al., 2017](#)). MOSES2.1 includes the Top-down Representation of Interactive Foliage and Flora Including Dynamics (TRIFFID) vegetation dynamics model ([Cox, 2001](#)) and represents each grid box as a mixture of the five TRIFFID vegetation types (broadleaf trees, needleleaf trees, temperate C3 grass, tropical C4 grass, and shrubs) and non-vegetated surface types, such as bare soil and land ice. MOSES2.1 calculates carbon fluxes (e.g., the terrestrial net primary productivity) for each vegetation type every 30 min as a function of climate and atmospheric CO₂ concentration from a coupled photosynthesis/stomatal-conductance scheme ([Cox et al., 1998](#)), which utilises existing models of leaf-level photosynthesis in C3 and C4 plants. The vegetation types respond differently to climate and CO₂ forcing and impact differently on the physical properties of the land surface, i.e., possessing different aerodynamic roughness lengths and albedo properties.

The TRIFFID model defines the state of the terrestrial biosphere in terms of soil carbon and the structure and coverage of five different plant functional types (PFTs) within each model grid box. Using the accumulated fluxes in MOSES2.1, TRIFFID calculates the areal coverage, leaf area index (LAI), and canopy height of the existing vegetation types and updates the five PFTs, the bare soil fraction, and soil carbon every 10 days. All vegetation types can co-exist within the same grid box, each possessing a fractional coverage equivalent to the population size. The land cover evolves dynamically based on competition between the vegetation types, which is modelled using a Lotka-Volterra approach ([Case, 2000](#)) and a tree-shrub-grass dominance hierarchy due to their height. The simulated vegetation in each grid box feeds back into the climate system in several ways, principally through evapotranspiration from the canopy, alteration of surface albedo, and alteration of mixing at the boundary layer between the surface and the atmosphere due to changes in roughness length.

Comparing the dominant PFT in the model to a reconstruction of pre-industrial vegetation, the HadCM3B-TRIFFID captures the true overall pattern, with several errors in the extent and exact location, such as expansion too far of broadleaf trees in the tropics, especially in the Southern Hemisphere, underestimation of grasses globally, and overestimation of the shrub at high latitude ([Valdes et al., 2017](#)). In part, these biases are due to the simplicity of the vegetation model, but a significant component also arises from the biases of the climate model itself.

2.2. Experimental design

[Armstrong et al. \(2019\)](#) implemented 42 snapshot simulations extending back to 60 ka BP, where 0 ka BP refers to the year 1950, using the HadCM3B-M2.1 model. The 30 ka BP experiment in that study was shown to demonstrate millennial-scale climate oscillations. Here, we run a 6185-year simulation utilising the same 30 ka BP boundary conditions; these are the orbital parameters (eccentricity of 0.01690, obliquity of 22.255° , and precession of -0.009), solar constant (1361.0 W m^{-2}), and atmospheric trace gases (CO₂ at 200 ppm, CH₄ at 397 ppb, N₂O at 200 ppb, with chlorofluorocarbons at 0). The prescribed orbital parameters are taken from ([Berger et al., 1998](#)). Atmospheric CO₂ concentration is from the Vostok Ice core ([Louergue et al., 2008](#); [Petit et al., 1999](#)), and both N₂O and CH₄ concentrations are from the EPICA Dome C ice core ([Spahni et al., 2005](#)).

The surface boundary conditions are derived from the ICE-5G continental ice sheet reconstructions (i.e., Greenland, Laurentide, Fennoscandian, and Antarctic ice sheets) ([Peltier, 2004](#)) and their associated topography, land-sea mask and bathymetry ([Fig. S1](#)). However, because the ICE-5G reconstruction has data up to only 26 ka BP, we have to calculate the older ice sheets from the equivalent ice volume/sea level. For example, the sea-level depression at 30 ka BP is compared to the sea level during the deglaciation, where they are the same the ice extent is inferred to be the same as that simulated by ICE-5G but for 30 ka BP. This approach is the same as [Davies-Barnard et al. \(2017\)](#) and [Armstrong et al. \(2019\)](#). There are limitations as ice sheets show different structures during decay and growth phases, but it likely provides a better approximation of the ice area than other methods ([Singarayer and Valdes, 2010](#)).

All boundary conditions are held constant throughout the simulation so that the observed oscillation arises from a set of spontaneous self-sustaining feed backs.

2.3. Methods

This study investigated large-scale and regional-scale changes in climate and vegetation associated with DO-like oscillations. The target areas were summarised in [Fig. S2](#).

All simulated time-series data were low-pass filtered with a half-period of a 200-year time window to remove high-frequency variability and catch the long-term trend.

We evaluated the robustness of spatial patterns regarding simulated climate and vegetation variations associated with DO-like warming using Greenland interstadial (GI) anomalies from Greenland stadial (GS). In our simulation, the twenty different climate and vegetation anomalies that combine four GIs and five GSs are available (See [Section 3.1.1](#)). The definitions of GS and GI are also in [Section 3.1.1](#). This study defines a robust response as the same signal (i.e., all positive or all negative) with all the twenty anomalies.

To investigate the tropical hydrological cycles associated with DO cycles, particularly ITCZ and monsoons, we used the precipitation centroid (P_{CENT}) and several monsoon indices in addition to precipitation changes ([Section 3.1.4](#)). P_{CENT}, defined by [Frierson and Hwang \(2012\)](#), is a metric for the location of the ITCZ-tropical precipitation maximum. This study calculates the P_{CENT} as the median of the zonal average precipitation from 25°S to 25°N . The simulated precipitation is interpolated to a 0.1° grid over the tropics to allow P_{CENT} to vary at increments smaller than the original model grid sizes. Meanwhile, various monsoon indices have been proposed considering the role of regional Hadley circulation and

Walker circulation. In this study, summer monsoon indices using zonal winds at 850 hPa level are selected for the Indian monsoon (Wang and Fan, 1999), East Asian monsoon (Wang et al., 2001), Australian monsoon (Kajikawa et al., 2010), and South American monsoon (Gan et al., 2005). The methodology of monsoon indices is referred to in each original paper. Each monsoon index suggests the intensification of the monsoon itself and the migration of ITCZ around each monsoon region, representing changes in moisture to the land area from the ocean (Gadgil, 2018).

3. Results and discussion

3.1. Climate variations

3.1.1. Simulated near-surface air temperature in Greenland

Fig. 1a shows simulated annual mean near-surface air temperature variations at the North Greenland Ice Core Project (NGRIP) site. This study defines simulated Greenland stadials (GSs) and Greenland interstadials (GIs) as follows. The time series of the

simulated near-surface temperature at the NGRIP site was low-pass filtered with a half-period of a 200-year time window. Each local warmest period based on the 100-year mean is GI, and each local coldest period based on the 300-year mean (the 200-year average for the first coldest period) is GS. Thus, this simulation includes five GSs and four GIs. The simulated near-surface temperature in Greenland from GSs to GIs increases by 7.1 ± 2.5 °C. The magnitudes of warmings are comparable to DO 6 (about 9.5 °C) and DO 9 (about 6.5–8 °C), the smallest temperature changes in the observed DO events (Kindler et al., 2014) (Fig. 1b–d). However, the simulated warmings are not as abrupt as in the observations and are slower than other simulations (e.g., Peltier and Vettoretti, 2014). Armstrong et al. (2022) discuss this and suggest it may be related to the relatively simple sea ice model in HadCM3B.

The features recognised as DO cycles are (a) the sawtooth-shaped oscillations observed in oxygen isotope $\delta^{18}\text{O}$ time series from Greenland ice cores (Kindler et al., 2014), with the concentration of $\delta^{18}\text{O}$ in ice cores interpreted as a qualitative proxy for the surface air temperature, (b) the changing frequency of DO cycles

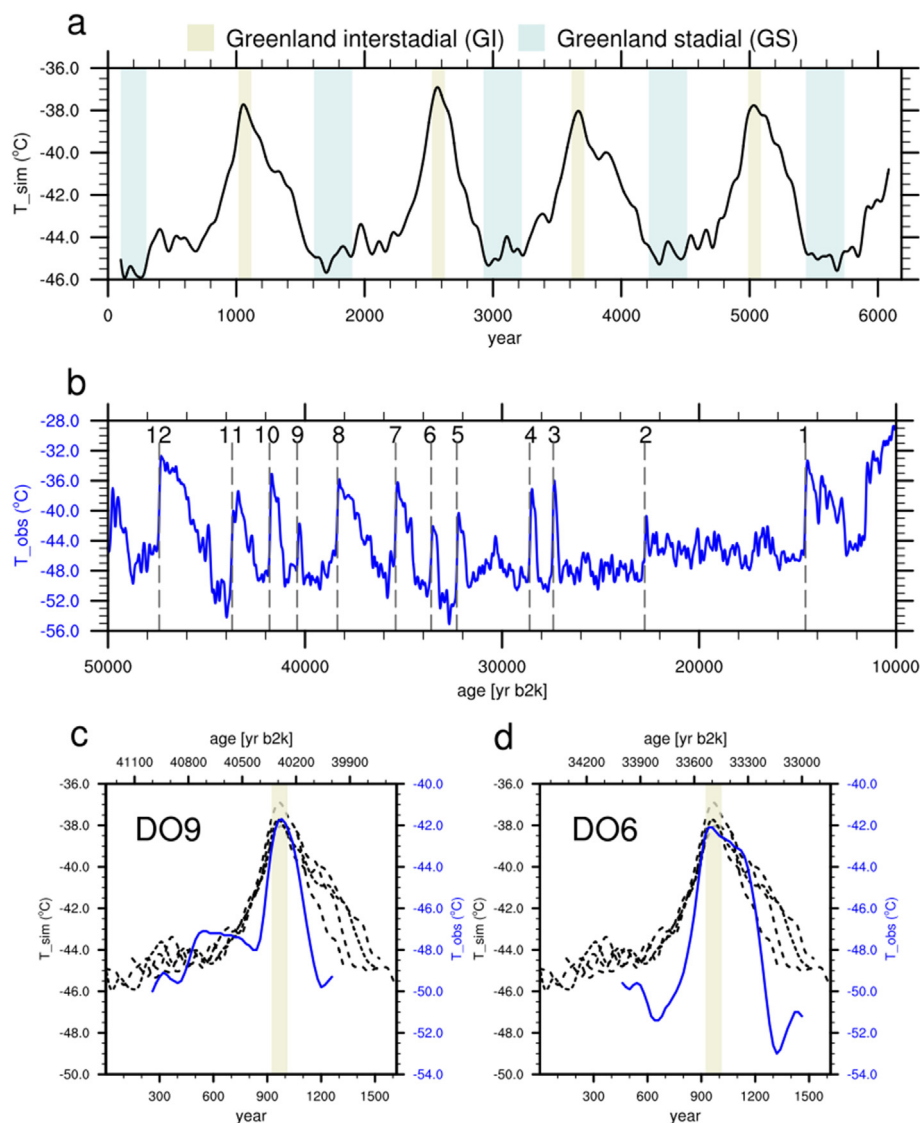


Fig. 1. Simulated annual mean near-surface air temperature in Greenland (a), NGRIP temperature reconstruction between 10 and 50 kyr b2k on the ss09sea06bm timescale from Kindler et al. (2014) with DO numbers (b) and each temperature variation of DO9 (c) and DO6 (d). The simulated temperature was low-pass filtered with a half-period of a 200-year time window. Dash lines in (c–d) present the simulated temperature variations from (a).

(Schulz, 2002), and (c) the observed antiphase relationship between the two hemispheres (Buizert et al., 2015). Our unforced glacial simulation reproduces sawtooth-shaped oscillations, characterised by rapid warming followed by progressive cooling, with a timescale of ca. 1500 years. This simulated oscillation frequency is compatible with the observed DO cycles between 60 and 20 ka BP (Andersen et al., 2004; Dansgaard et al., 1993). The observed millennial-scale climate oscillations are characterised by abrupt warming events in the North Atlantic region and more gradual temperature changes in Antarctica (Buizert et al., 2015; Wolff et al., 2010), possibly resulting from changes in the interhemispheric heat transport due to the AMOC variations (the Bipolar Seesaw theory; Barker et al., 2011; Knutti et al., 2004; Stocker and Johnsen, 2003). The simulated temperature in Antarctica gradually increases during GSs and decreases during GIs, and their amplitude in Antarctica is much smaller than in Greenland (Fig. S3).

3.1.2. Large-scale climate oscillations associated with DO-like cycles

Fig. 2a–b shows the area-weighted average anomalies from the long-term mean (based on the entire 6185-year period) for annual mean simulated near-surface temperature and precipitation for the Northern Hemisphere extratropics (NHEXT, 25°N–90°N), the Northern Hemisphere tropics (NTROP, 0°–25°N), the Southern Hemisphere tropics (STROP, 25°S–0°), the Southern Hemisphere extratropics (SHEXT, 60°S–25°S). Changes in the regional-scale seasonal mean precipitation are shown in Fig. 2c–f and Fig. S4, and the seasonal temperature changes are shown in Fig. S5.

The large-scale temperature variations are small but with distinct features in each area (Fig. 2a). The annual temperature variations in the NHEXT and NTROP correlate with the variations in Greenland (more than 0.9 in the cross-correlation coefficient, xcor). The annual mean temperature rises between GSs and GIs in the NHEXT (1.5 ± 0.3 °C) are larger than in the other regions, and that

extent declines as one moves away from the northern North Atlantic. On the other hand, the temperature change in the SHEXT is out of phase with one in Greenland, but it is similar to Antarctica, with gradual increases in temperature toward GIs and declines in temperature after GIs. Moreover, changes in simulated annual precipitation in the NHEXT and NTROP show a specific trend; more precipitation during GS periods and less precipitation during GI periods (Fig. 2b; more than 0.9 in the xcor). As a result, these precipitation variations correlate with temperature changes in the Northern Hemisphere. Rates of precipitation changes are similar between the NHEXT and NTROP, while temperature changes in the NHEXT are larger than in the NTROP. Thus, the precipitation changes in NTROP are expected to result from changes in dynamic, such as the Hadley circulation and Walker circulation, rather than thermodynamic factors, such as the Clausius-Clapeyron relationship.

Most regional target areas also show a similar temporal trend to the large-scale areas, but their amplitudes differ between the seasons and locations even if they have the same latitudinal bands (Fig. 2c–f; Fig. S4). Some monsoon regions in the Northern Hemisphere, such as the Indian subcontinent (IN) and the Sahel (SHL), show abrupt increases in boreal summer (June–July–August: JJA) precipitation during GIs. Central America and northern South America (CNSA), the location of the northern end of the Atlantic tropical rain belt, also show abrupt increases in boreal summer precipitation during GI periods. On the other hand, the Amazon basin (AMZ), South Africa (SA), and Australia (AU) show increases in the simulated austral summer (December–January–February: DJF) precipitation during GIs. Changes in summer precipitation in each Hemisphere between GIs and GSs are particularly large in the Northern Hemisphere monsoon regions (e.g., IN, SHL) and around the northern and southern ends of the ITCZ (e.g., CNSA and AMZ).

Although the amplitude is small, our simulation also shows that

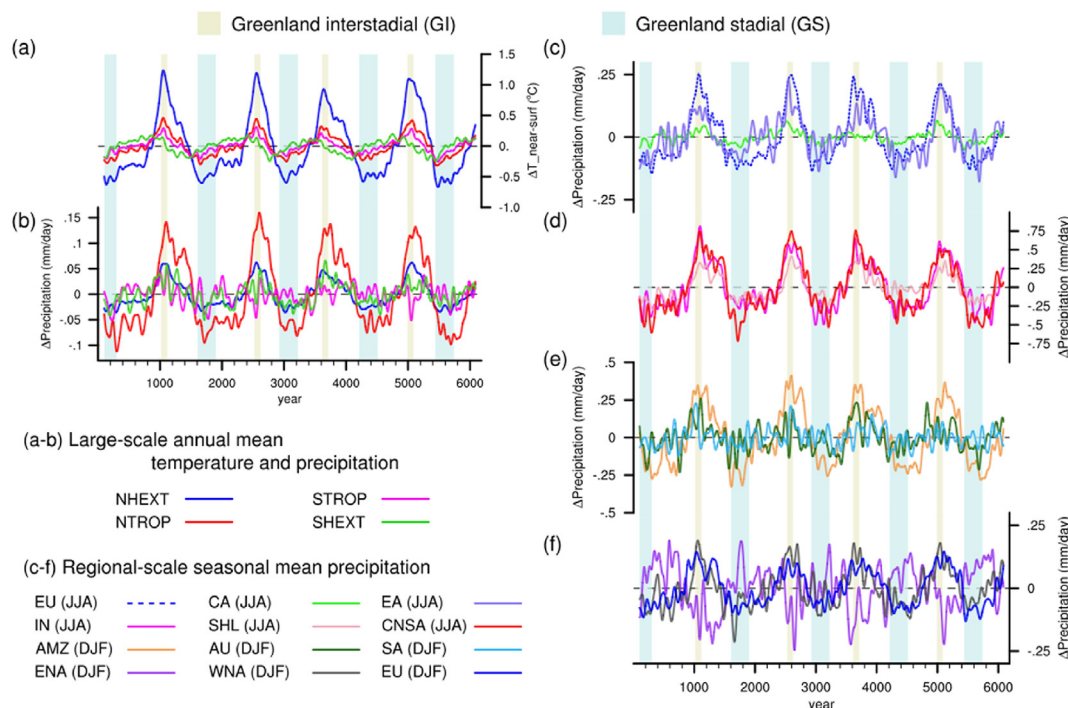


Fig. 2. Simulated large-scale annual mean near-surface air temperature and precipitation anomalies from the long-term mean (a–b) and simulated regional-scale seasonal mean precipitation anomalies from the long-term mean (c–f). All data was low-pass filtered with a half-period of a 200-year time window. Regional areas are Europe (EU), Central Asia (CA), East Asia (EA), the Sahel (SHL), the Indian subcontinent (IN), Central America and northern South America (CNSA), the Amazon (AMZ), Australia (AU), South Africa (SA), eastern North America (ENA), and western North America (WNA). The specific information for the regional areas is in Fig. S2.

specific wintertime precipitation changes among western North America (WNA), eastern North America (ENA), and Europe (EU); increases in precipitation in EU and WNA and decreases in precipitation in ENA during GIs (Fig. 2f). Millennial-scale temperature changes are similar there (Fig. S5), but precipitation changes are reversed on both sides of the North American continent and in the North Atlantic.

3.1.3. Large-scale climate changes associated with DO-like warmings

With DO-like warming events, simulated near-surface air temperature increases in many parts of the Northern Hemisphere, particularly in the NHEXT, throughout the year, but the warming in boreal winter is larger than in boreal summer (Fig. 3a). In contrast, the temperature changes in the Southern Hemisphere, particularly in oceans, are less robust and much smaller than in the Northern Hemisphere; they are either not directly affected by the DO-like warming or are temporally (phase in the time series data) displaced. The largest temperature responses due to DO-like warming occurs in the northern North Atlantic Ocean and its coastal areas: Greenland, western Europe, and eastern North America. The large warming also happens over Beringia. The simulated wintertime warming over the North Atlantic and Beringia mainly results from a large reduction of sea-ice cover (Fig. S6). Some evidence shows that the DO cycles were characterised by large changes in sea-ice cover in the North Atlantic during the last glacial period (Jensen et al., 2018; Masson-Delmotte et al., 2005; Pedro et al., 2022; Sadatzki et al., 2019, 2020). The warming over east Siberia is also consistent with a lake sediment record in Lake Baikal, East Central Siberia, showing a teleconnection between the North Atlantic Ocean and East Central Siberia, coinciding with Heinrich events and DO events (Grygar et al., 2006).

The simulated precipitation shows specific responses associated with DO-like warming in some regions (Fig. 3b). The annual precipitation increases in the northern-eastern North Atlantic and decreases along the Gulf stream in the western North Atlantic, but the wintertime responses are much larger than the summertime. The wintertime precipitation also decreases along with the Kuroshio Current in the western North Pacific. The tropical rain belt migrates northwards over the tropical Atlantic, leading to more

precipitation in Central America and northern South America and less precipitation over the equatorial Southern Hemisphere, especially ocean regions. This influx of freshwater into the equatorial Northern Hemisphere Atlantic strongly impacts the AMOC (Armstrong et al., 2022; Vellinga and Wu, 2004). The tropical precipitation also increases in the eastern equatorial Pacific while decreasing in the South Pacific Convergence Zone and along the North Pacific atmospheric river. The simulated wintertime precipitation increases in the terrestrial tropics (e.g., the Amazon Basin, the Congo Basin, and Sundaland), while the simulated summertime precipitation increases in the Northern Hemisphere monsoon regions, such as West Africa and the Indian subcontinent.

3.1.4. Hydrological cycles over the tropics

As mentioned above, changes in temperature and precipitation in the tropics have a similar time-series trend to temperature changes in Greenland. However, the change in precipitation is relatively large despite the slight temperature change. This section investigates the tropical hydrological cycles, particularly ITCZ and monsoon, associated with DO cycles using the precipitation centroid (P_{CENT}) and several monsoon indices (Fig. 4). The calculation methods are described in Section 2.3.

The zonal mean global P_{CENT} for the long-term mean state shows the seasonal latitudinal migration from $6.5^{\circ}\text{S} \pm 0.4^{\circ}$ in DJF to $5.4^{\circ}\text{N} \pm 0.4^{\circ}$ in JJA, and the annual mean location is at $0.9^{\circ}\text{S} \pm 0.6^{\circ}$. The ITCZ generally migrates towards a warming hemisphere on seasonal and longer timescales (Donohoe et al., 2013; Frierson and Hwang, 2012), and our simulation is consistent with those previous studies (Fig. S7). The global mean P_{CENT} moves northward during GIs and southward during GSs by $0.8^{\circ} \pm 0.6^{\circ}$, respectively, and these features are also shown for the regional ocean areas (Fig. 4a). The zonal mean P_{CENT} over the Atlantic shows much further and sharp northward shifts from GSs to GIs. In addition, while this northward shift is independent of seasons, the wintertime northward shift in the Pacific and Atlantic tends to be more pronounced than in summer (Fig. S8). The simulated ITCZ shifts northwards due to DO warming, resulting in intensified precipitation in the tropical North Atlantic, reducing surface salinity in the tropical North Atlantic, and enhancing evaporation from the tropical South Atlantic (Armstrong et al., 2017; Vellinga and Wu, 2004).

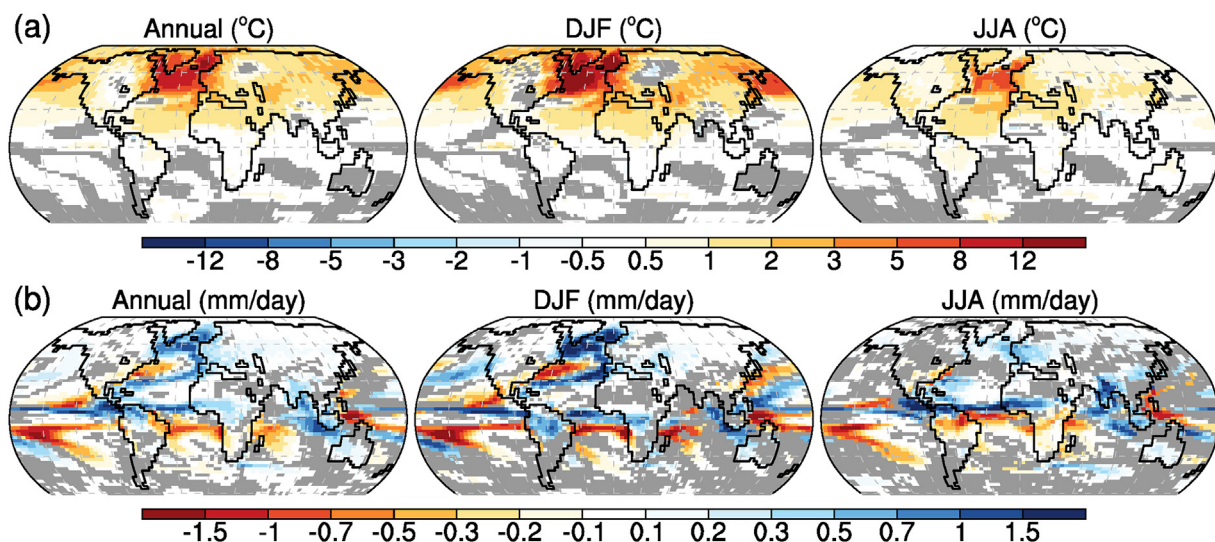


Fig. 3. Simulated annual and seasonal (DJF and JJA) mean near-surface air temperature (a) and precipitation (b) differences between the averaged GI and GS climate states. The colour scale means that all the 20 climate anomalies have the same responses (i.e., all positive or all negative) about each climate variables. Gray shade means no robust responses in the 20 anomalies.

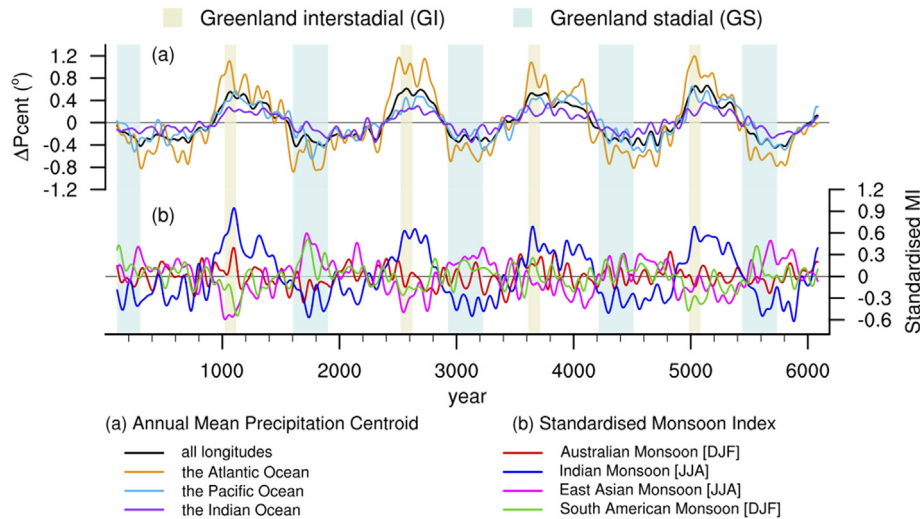


Fig. 4. Shift of the annual mean precipitation centre (degree, see text for definition) for the globe, the Atlantic Ocean, the Pacific Ocean, and the Indian Ocean relative to the long-term mean (a). Standardised monsoon indices over the four regions: Australia, India, East Asia, and South American (b). A positive means a northward shift of the ITCZ in (a) and strengthening monsoon in (b). The reference value of annual mean ITCZ location is $0.9^{\circ}\text{S} \pm 0.6^{\circ}$ for the globe, $0.6^{\circ}\text{S} \pm 1.1^{\circ}$ for the Atlantic Ocean, $4.2^{\circ}\text{N} \pm 0.9^{\circ}$ for the Pacific Ocean, and $2.4^{\circ}\text{S} \pm 0.6^{\circ}$ for the Indian Ocean.

After GI periods, surface ocean salinity in the tropical North Atlantic is reduced enough to weaken AMOC, shifting the climate into cold phases (i.e., GSs). These ITCZ shifts over the equatorial Atlantic influence the surface freshwater balance, surface ocean salinity, and, therefore, AMOC strength, including on centennial timescales (Armstrong et al., 2017; Vellinga and Wu, 2004).

Monsoons have been regarded as regional sea breeze circulations driven by land-ocean thermal contrast, especially in summer (Webster et al., 1998). However, the concept of the global monsoon system appeared (Trenberth et al., 2000; Wang and Ding, 2008), stating that the global monsoon can be viewed as a response of the coupled climate system to the annual cycle of solar insolation. The leading mode is a hemispheric anti-phase pattern of precipitation and circulation. Because all regional monsoons are bounded and synchronized by the solar forcing variation, the global monsoon system strongly relates to global-scale atmospheric and hydrological circulation, such as the Hadley circulation and ITCZ.

Based on the monsoon index using simulated 850 hPa westerlies (Fig. 4b), the Indian summer monsoon strengthens during GIs and weakens during GSs, positively related to the changes in Greenland temperature. In contrast, the South American monsoon index shows the opposite response to the Indian monsoon. These monsoon responses are also consistent with ITCZ migration associated with DO-like oscillation. However, the East Asian monsoon index showed the opposite response to the Indian monsoon, weakening during GI and strengthening during GS, despite being one of the Northern Hemisphere monsoons. This weakening monsoon index results from changes in westerlies (Fig. S9) over the western Pacific, leading to decreases in precipitation over the equatorial western Pacific Ocean, like a part of La Niña, despite increases in precipitation in southern China (Fig. 3b). Specific millennial-scale variations, as seen in the other monsoons, were not shown in the Australian summer monsoon (Fig. 4b). Meanwhile, changes in onshore precipitation (Fig. 2c–d) can be interpreted as indicating that DO-like warming also strengthens the summer monsoon in the Northern Hemisphere, including West Africa and East Asia, following the northward migration of the ITCZ. It should be noted that in the East Asian monsoon, the response varies depending on the index used.

3.2. Vegetation changes

3.2.1. Global vegetation distribution under a glacial period

Fig. 5a shows the simulated glacial vegetation distributions based on the GS mean state for 1400 years. The PFTs co-exist within the same grid box, and PFT types better suited to the environment occupy a larger area. The dominant PFT is a PFT with the largest fractional covering at each grid. Broadleaf trees spread across the tropics except for Australia, Indian subcontinent, and North Africa. There are substantial C4 grasses in Australia, the Indian subcontinent, and the Sahara-Sahel boundary. Needleleaf trees and shrubs are distributed in eastern North America, southwestern-southcentral Europe, and eastern Asia, but most of the shrubs are distributed around the areas for needleleaf trees. C3 grasses are distributed mainly in boreal regions where boreal forest or tundra is distributed under present-day climate conditions (Kaplan et al., 2003).

Fig. 5b shows the simulated global PFT fractional coverages in a climate space, which refers to the annual mean near-surface air temperature (MAT) and total annual precipitation (TAP) at a grid box. Each PFT exists in a relatively unique region of the simulated climate space. The broadleaf trees are abundant in warm (above 14°C in MAT) and wet conditions (more than 1000 mm in TAP). The needleleaf trees are abundant between 4°C and 12°C in MAT and more than 600 mm in TAP. C3 grass is found over a large amount of climate space but is abundant in cold and dry conditions, and C4 grass is most suited for warm and dry conditions. The shrub is most abundant in the range from -6°C to 4°C in MAT. The large fraction coverage of each PFT differs among the latitudinal bands because of competition from other PFTs.

This simulated DO-like warming is comparable to the observed DO9, one of the smallest temperature changes in the DO cycle (Fig. 1c). However, because it does not attempt to reproduce one specific DO event, the simulated temperature is much higher than the reconstruction. Thus, it is not useless to directly compare the simulated vegetation to the observed vegetation composition. On the other hand, the simulated vegetation responses to this DO-like millennial-scale climate variability are worth evaluating because the climate variability is reasonable.

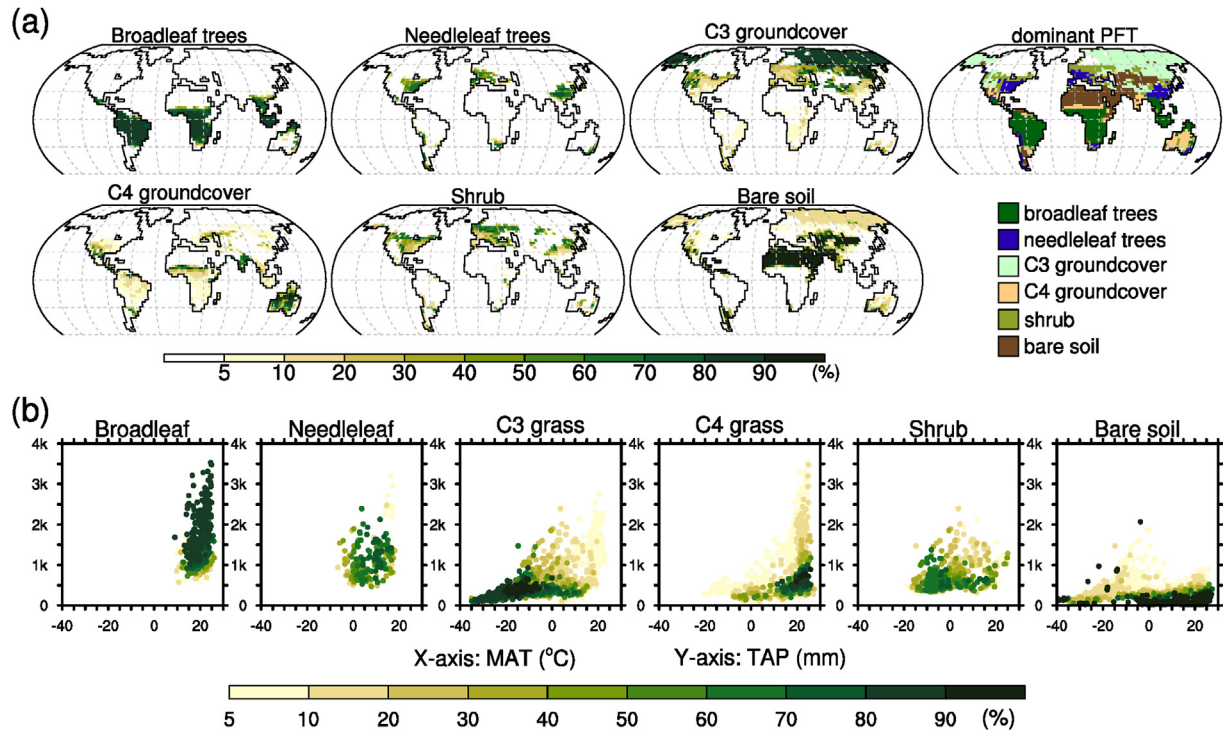


Fig. 5. Simulated fractional PFT coverage and the dominant PFT in Greenland stadials (a) and the PFT distribution within the climate space (in terms of annual mean near-surface air temperature (MAT) and total annual precipitation (TAP) (b)).

3.2.2. Large-scale vegetation oscillations associated with DO-like cycles

Fig. 6 shows the simulated annual mean PFT fractional coverage anomalies from their long-term mean state (Table 2) in the NHEXT, NTROP, STROP, and SHEXT. The large-scale variations associated with DO-like events are very small but demonstrate specific

responses at each latitudinal band. Regional-scale PFT variations are shown in Figs. S10–12.

The simulated fractional coverage of both shrub and needleleaf tree increases over the NHEXT during GIs and decreases during GSs (Fig. 6a). The changes in shrubs ($2.9\% \pm 0.4\%$) are much larger than in needleleaf trees, and their fractional coverage increases as

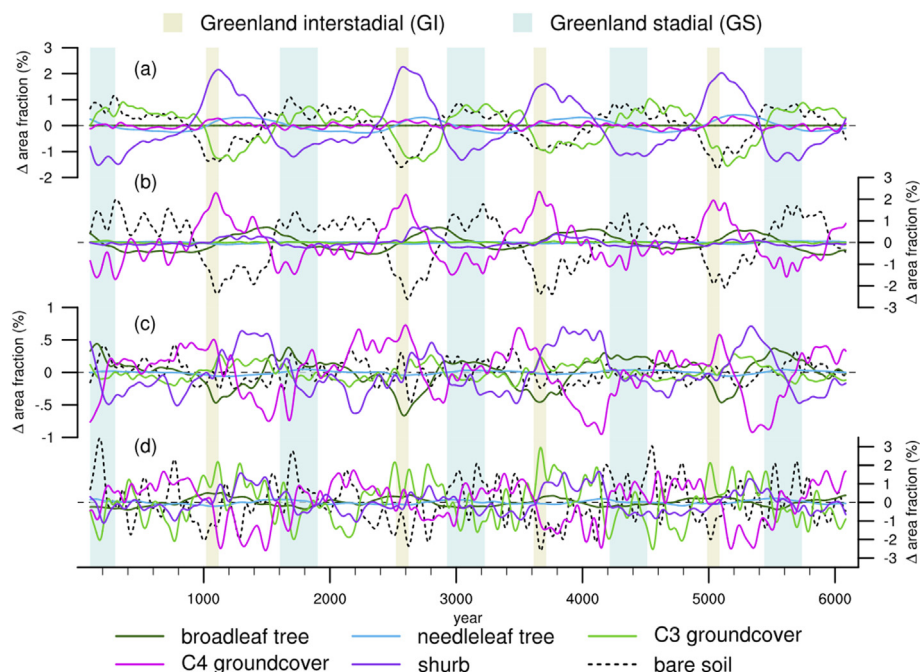


Fig. 6. Changes in simulated fractional PFT coverage associated with DO-like oscillation over the NHEXT (a), NTROP (b), STROP (c) and SHEXT (d). The all values are area-weighted average anomalies from the long-term mean.

Table 2

The long-term mean large-scale fractional PFT cover (%).

Area/PFTs	PFT1 ^a	PFT2 ^a	PFT3 ^a	PFT4 ^a	PFT5 ^a	PFT8 ^a
NHEXT ^b	0.0	8.4	43.2	4.5	16.1	27.2
NTROP ^b	30.7	3.2	2.4	20.7	2.1	39.9
STROP ^b	66.3	2.4	5.1	19.0	3.8	3.2
SHEXT ^b	10.2	19.4	13.0	21.3	11.3	24.8

^a PFT1: broadleaf tree, PFT2: needleleaf tree, PFT3: C3 groundcover, PFT4: C4 groundcover, PFT5: shrub, and PFT8: bare soil.

^b Total area: 7.10×10^7 km² for the NHEXT, 3.32×10^7 km² for the NTROP, 2.76×10^7 km² for the STROP, and 1.15×10^7 km² for the SHEXT.

temperature and precipitation increase. Due to differences in PFTs' growth timescale (several decades years for shrubs and several hundred years for needleleaf trees) in TRIFFID, peaks of the PFTs expansion are delayed from the peak of temperature and precipitation (Hughes, 2003). On the other hand, simulated C3 grasses shrink sharply during GIs and expand gradually from GIs to GSs, and the amplitude is $1.6\% \pm 0.5\%$. As a result, the fractional coverage of bare soil changes by $2.0\% \pm 0.6\%$ during DO-like cycles, with more vegetated cover during GIs relative to GSs.

Over the NTROP (Fig. 6b), the simulated fractional coverage of C4 grasses quickly expands during GIs and gradually shrinks during GSs, with a variation of $2.8\% \pm 0.9\%$. This response correlates to changes in large-scale temperature and precipitation over the TROP; as the temperature rises and precipitation increases, C4 grasses expand. Compared to C4 grasses, the responses of shrub and broadleaf trees are similar but much smaller, and the peaks of their expansion shift backwards because of their growth timescale (Hughes, 2003). The fractional coverage of bare soil in the NTROP changes by $2.8\% \pm 1.0\%$ during DO-like cycles, with more vegetated cover during GIs relative to GSs.

Changes in fraction PFT cover in the STROP are much smaller than in the other regions, and their trends differ from the Northern Hemisphere (Fig. 6c). C4 grasses quickly expand during GSs, gradually expand or almost stabilise from GSs to GIs and shrink after GIs. On the other hand, shrubs expand over the pre- and post-GI period, their expansion stabilises between GIs and GSs, and they shrink before and during GSs. Broadleaf trees shrink during GIs and expand during GSs, the phase position is offset from that of shrubs by c.a. 400 years, and thus the peak of the expansion-contraction roughly coincides with GS-GI periods. C3 grasses expand from GIs to GSs and shrink from GSs to GIs, and the response is opposite to one in the NHEXT.

Long-term trends of PFT fractional changes in the SHEXT are similar to the STROP except for the broadleaf trees (Fig. 6d). The fractional coverage of C3 grasses and shrubs expands during GIs and shrinks during GSs, while the responses of C4 grasses are the opposite. Variabilities of the C3 and C4 grasses are high frequency, as is the fluctuation of the SHEXT precipitation. On the other hand, broadleaf trees expand during GIs and shrink during GSs, and the trend is opposite to one in STROP.

3.2.3. Large-scale vegetation changes associated with DO-like warmings

Here, we investigate the robustness of spatial variations for fractional covering of PFTs due to DO-like events and the changes in the climate space (Fig. 7). When both climate and vegetation variations have robustness, the climate factors can be interpreted to influence the vegetation changes. Due to the different growth timescale of each PFT (i.e., a few years for C3–C4 grasses, several decades for shrubs, and several hundred years for trees) in TRIFFID, this section focuses more on the relatively short response of vegetation to DO-like warming. The regional changes in climate spaces are shown in Figs. S13–15.

As shown in Fig. 6a–b, the vegetated area during GIs, especially in the Northern Hemisphere, expands more than during GSs. The fractional coverage of bare soil during GIs robustly decreases (i.e., vegetated coverage increases) in eastern Europe, central Asia, eastern Siberia, western-central Australia, and some Northern Hemisphere monsoon areas such as the Indian subcontinent and West Africa. In contrast, the bare soil increases (i.e., the vegetated coverage decreases) in southwestern North America and the Horn of Africa. Large-scale changes in bare soil depend on precipitation variations alone (Fig. 7b).

Although these are small but robust changes in PFTs, the simulated changes in large-scale dominant PFT associated with DO warming are not changed (Fig. 7a). The result is similar to the observed biome changes associated with the DO6 events (about 9.5°C warming), which does not show biome changes from the observed GS 6/7 to the observed GI 6 except for the Pacific Northwest, where boreal forests changed into temperate forests and the Mediterranean region, where the herbaceous and shrub changed into open sclerophyll forest/woodlands (Harrison and Sánchez Goñi, 2010). Although there are differences in the baseline climatology for the observed and simulated temperatures during Greenland stadials, the increase in the simulated temperature around 7°C does not cause a large-scale change in the dominant biome in the glacial condition.

The change in the simulated broadleaf trees is very small, decreasing in northeast Brazil and southeast Africa, including Madagascar, while increasing in northern South America, southeast China, and New Zealand. The broadleaf trees increase as precipitation increases in the NHEXT and the tropics. The simulated C4 grasses displace the broadleaf trees in northeast Brazil and southeast Africa, potentially because of a decline in austral winter precipitation (Fig. 3b). The change in the simulated needleleaf trees is also small, but they increase over southwest Europe, central China, and Patagonia and decrease in the eastern United States. The needleleaf trees in the NHEXT increase as temperature and precipitation increase while possibly decreasing as temperature increases in the tropics (Fig. 3b). Because the growth timescale of both simulated trees is much greater than the other simulated PFTs, such as the C3–C4 grasses and shrubs, the changes in trees associated with DO-like warming are smaller than C3–C4 grasses and shrubs (Fig. 6). Moreover, as Fig. 7b shows, changes in trees over the NHEXT, NTROP, and STROP result from variations in both temperature and precipitation associated with DO-like events, while the cause of changes in trees over the SHEXT is ambiguous.

The simulated C3 grasses increase over the boreal region, central Asia and eastern Europe, and western-southern Australia and decrease in western-central Europe, parts of eastern Europe, and East Asia. Because only the simulated C3 grass is present in the glacial boreal region, the increase in the C3 grasses directly replaces the decrease in the bare soil. The C3 grasses decrease as temperature and precipitation increase in the NHEXT, except in central Asia. In contrast, changes in the C3 grasses in other regions do not simply depend on variations in annual temperature and precipitation because of competition with the simulated C4 grass and shrubs. On the other hand, the simulated C4 grasses increase in the Indian subcontinent, the Sahel, the Amazon basin, western Asia, northeast Brazil, and central Australia while decreasing in eastern Europe and parts of central-south Australia. Both simulated C3 and C4 grasses can exist over the tropics and mid-latitudes, but the C4 grasses use water more efficiently than C3 grasses, so requires less water to produce the same amount of biomass (Essery et al., 2001; Valdes et al., 2017). The increases in the C4 grasses depend on different climate factors for each region: an increase in annual temperature and precipitation over the NHEXT, particularly in central Asia, an increase in annual precipitation over the NTROP, and an increase in

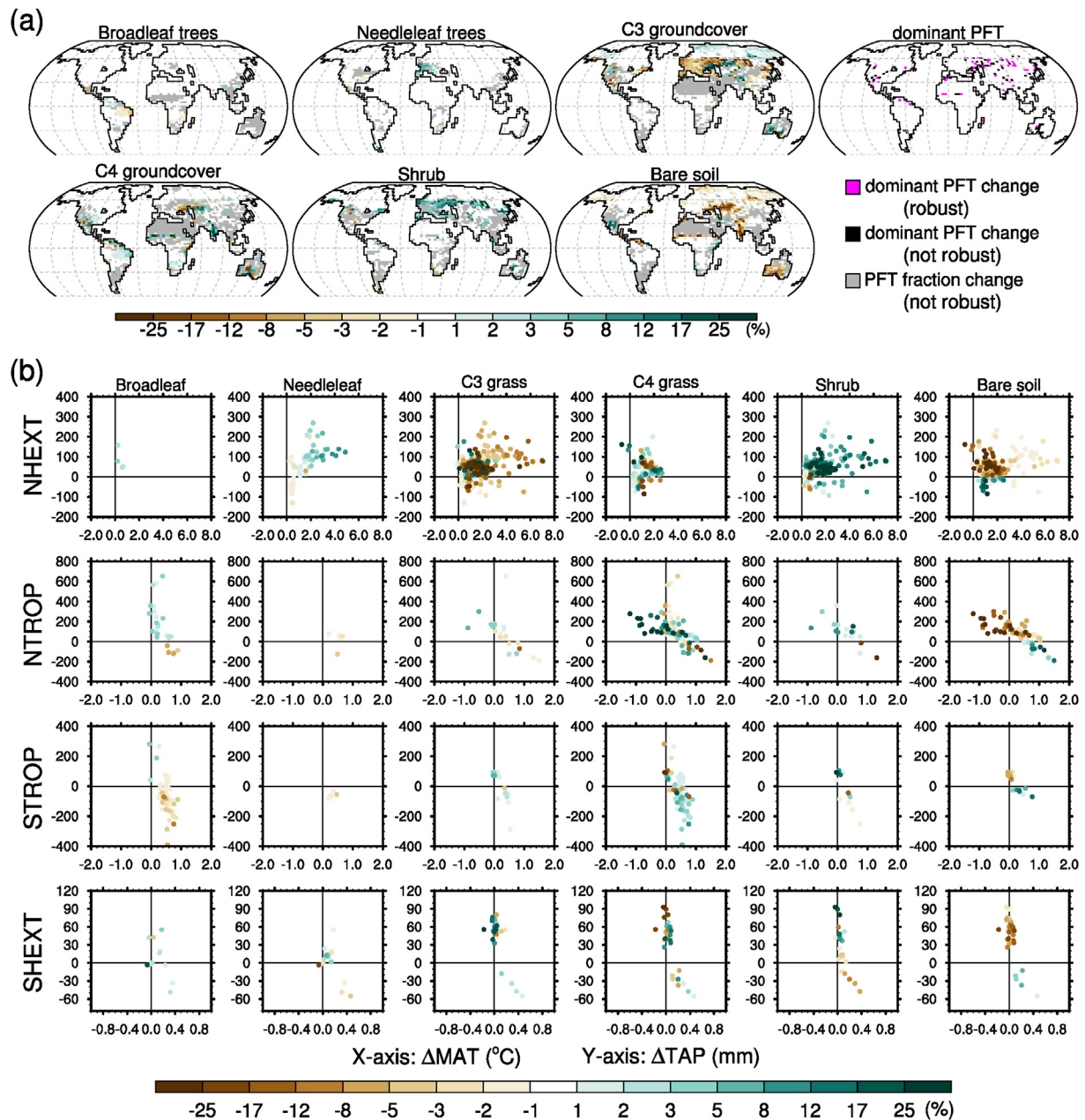


Fig. 7. Differences of simulated PFT fractional coverage between the averaged GI and GS periods (a). Changes in vegetation distributions within the climate space in terms of annual mean near-surface air temperature and total annual precipitation differences between the averaged GI and GS periods (b).

annual temperature over the STROP. Finally, shrubs increase over mid-latitude Eurasia, the Pacific Northwest, Southeast Canada, South Alaska, and central Australia. This shrub change is a response to an increase in temperature over the NHEXT and precipitation over the NTROP, STROP, and SHEXT.

4. Comparison to proxy climate data

4.1. ITCZ migration

Spatially limited palaeoclimate proxy data does not show global-scale ITCZ variations but indicates globally coherent regional migrations along the DO cycles. Speleothem and sediment records from the tropical Atlantic and Indo-Asian regions (Deplazes et al., 2013; Kathayat et al., 2016; Peterson et al., 2000; Wang et al.,

2004) indicate a northward shift of ITCZ at the timing of DO events, consistent with our simulation. Stalagmites from Borneo responded more strongly to Heinrich Events than DO events, indicating decreases in rainfall (i.e., southward ITCZ migration has been suggested) coincident with high-latitude cooling (Carolin et al., 2013; Partin et al., 2007). Adolphi et al. (2018) also show that Greenland ice-core and four speleothem records from three different tropical-subtropical regions (Hulu-Dongge Cave in China, Cueva del Diamante and El Condor Cave in Amazonia, Sofular Cave in Turkey) shows that atmospheric circulation changes in the tropics happened synchronously with DO events within the cross-dating uncertainties about 190 years, highlighting that the ITCZ migrated synchronously over the different ocean basins and continents. Models also simulate latitudinal ITCZ migration in response to interhemispheric temperature gradients (Chiang and Bitz, 2005;

Donohoe et al., 2013; Singarayer et al., 2017). Because temperature changes over the Southern Hemisphere are less pronounced than over the Northern Hemisphere during the last ice age, temperature changes over the Northern Hemisphere, especially in high-latitude regions, strongly influence the interhemispheric temperature contrast (Blunier et al., 1998), potentially leading to the millennial-scale ITCZ migration. Thus, the model simulations of the ITCZ are in broad agreement.

4.2. Monsoon intensity changes

Paleoclimate proxy records indicate a strong relationship between Greenland temperature and global monsoon intensity (Table 1). Several ocean climatic proxies of the Indian monsoon, such as laminated sediments from the Bay of Bengal and the Arabian Sea, show that changes in the Indian summer monsoon correlated to the changes in Greenland temperature (Deplazes et al., 2013, 2014; Schulz et al., 1998; Zorzi et al., 2022). Moreover, a stalagmite oxygen isotope record from northern China and a speleothem record from south-western China indicate that East Asian monsoon strengthened associated with DO events (Dong et al., 2018; Duan et al., 2014; Mingram et al., 2018; Wang et al., 2001), and Kathayat et al. (2016) show strong coherence between Indian and East Asian monsoons. Pollen records in equatorial west Africa indicate arid conditions associated with the Heinrich events (Lézine et al., 2019; Mulitza et al., 2008), and West Africa during Greenland interstadials can be interpreted as wetter than Greenland stadials. Speleothem-derived proxy of the South American summer monsoon (Kanner et al., 2012) and ocean sediment (including Iron/Potassium ratio) proxy of the South African climate (the south of the South African monsoon area; Ziegler et al., 2013) show that Southern Hemisphere summer monsoons were anti-correlated to the changes in Greenland temperature, leading to dry condition according to DO events. Our simulated onshore precipitation shows that Northern Hemisphere monsoons in India, West Africa, and East Asia intensify associated with DO-like warming, consistent with the proxy data. Moreover, our simulated monsoon index using 850 hPa westerlies for South American monsoon is also compatible with the proxy record, showing weakening monsoon associated with DO events.

Moreover, several proxy records show a strong correlation between ITCZ position and monsoons (Cheng et al., 2012; Deplazes et al., 2013); during the Greenland interstadials/stadials, the ITCZ shifted northwards/southwards, and Indian and East Asian monsoons strengthened/weakened. The consistency of ITCZ and monsoon variations may be evidence that monsoon variations indicate rainfall redistribution within the tropics and subtropics, with a northward displacement of the ITCZ implying increased rainfall further north and decreased rainfall further south (Cheng et al., 2012; Gadgil, 2018). Simulated millennial-scale variabilities of the Greenland temperature, ITCZ migration, and monsoon intensity are consistent with observations. The monsoon variations are based on the concept of the global monsoon system because summer temperatures in the tropics and subtropics are lower.

4.3. The bipolar seesaw

Our simulation represents the millennial-scale antiphasing temperature oscillations in Greenland and Antarctica (Fig. S3), consistent with the bipolar seesaw theory generally hypothesised to originate from AMOC oscillations. A sudden weakening of thermohaline circulation in the North Atlantic due to freshwater influx results in a reduction in the northward heat transport to the Northern Hemisphere and a reduction of heat loss in the Southern Hemisphere. Thus, the Northern Hemisphere cools down while the

Southern Hemisphere heats up. This heat build-up in the Southern Hemisphere is presumed to take some time, hence the slower response of Antarctica. Buizert et al. (2015) indicate that abrupt Greenland warming occurred about 200 years earlier than the corresponding Antarctica cooling onset, while Greenland cooling occurred about 200 years earlier than the corresponding onset of Antarctica warming. Then, when the deep-water formation strengthens, the meridional heat transfer resumes, and the Northern Hemisphere warms while the Southern Hemisphere cools. In contrast, our simulation represents that the Antarctic cooling transition may, in some events, begin before the Greenland interstadial warming transition (Fig. S3), similar to the timing seen by a simulation in Peltier and Vettoretti (2014) and the EDML ice core (Stenni et al., 2010), but not the timing that Buizert et al. (2015) suggested. The observed timing was based on the average of DO3–DO18 events, and not all events had such a clear trend, but the timing discrepancy between data and model is possible because the abruptness of the simulated warming in Greenland is less than the observed one (Fig. 1c–d).

4.4. Vegetation changes associated DO-like oscillations and warmings

Europe, affected downstream by North Atlantic climate variations, potentially provides robust evidence of past vegetation changes in response to the DO cycle. Pollen records indicate that interstadials (i.e., warm and humid periods in Europe) promoted the establishment of grassland (Poaceae and Cyperaceae) and low shrubs (*Salix herbacea*, *Betula nana*, and *Juniperus*) in northwestern Europe, woody vegetation (shrub- and forest-tundra) in northeastern Europe, open boreal forest (with *Pinus*, *Picea*, *Larix*, and *Betula*) in western Europe, and open temperate forest dominated by deciduous *Quercus* and associated thermophilous trees in southern Europe (Fletcher et al., 2010; Harrison and Sánchez Goñi, 2010). Our simulation shows robust vegetation changes associated with DO warmings in Europe, particularly in western regions: expansion of both shrubs and needleleaf trees and reduction of C3 grass during the transition periods to GIs (Fig. 7a).

Pollen records from the European continent also suggest a southward displacement of the northern limits of temperate forests at around 45°N in western and central Europe, transitioning from open temperate forest to tundra across a narrow latitudinal band of around 15°N (Fletcher et al., 2010). At northern latitudes above 50°N, the pollen records suggest the episodic development of woody vegetation under warm conditions. The simulated northern limits of needleleaf trees are around 45°N, and shrubs distribute up to 60°N (Figs. 5a and 7a), and the limits do not change between GI and GS periods, but their PFT fractional areas increase in Europe. On the other hand, the pollen records suggest the presence of trees above 50°N in northeastern Europe, where interstadial climatic conditions were suitable for tree development at high latitudes. The TRIFFID DGVM does not simulate needleleaf trees above 50°N in northeastern Europe but shrubs and C3 grasses due to the glacial climate and the low atmospheric CO₂.

The vegetation response in North America was complex and variable. Pollen data show several responses to the millennial-scale climate variations due to DO and Heinrich climate variability but no correlation of the vegetation changes, especially in the Pacific Northwest, with specific climatic events in Greenland (Jiménez-Moreno et al., 2010). In contrast, those pollen records indicate that the Colorado Plateau and southwestern North America were warmer-wetter in GIs than in GSs but relatively cooler-drier in Florida. Our simulation does not show the strong vegetation response associated with DO-like oscillations in western North America (WNA in Fig. S10), but a decrease in C3 grasses and an

increase in shrubs in the Pacific Northwest, which are also consistent with the observation. On the other hand, our simulation shows the strong vegetation response in eastern North America (ENA in Fig. S10) due to relatively dry conditions during GI winter periods (Fig. 2f). Vegetation-inferred climate changes in southern Florida and western North America indicate the antiphase between the two regions (Donders et al., 2011; Grimm et al., 2006; Jiménez-Moreno et al., 2010), and our simulation simulates this antiphase of precipitation variation between western and eastern North America associated with DO-like oscillation. Moreover, the simulated millennial-timescale climate and vegetation asymmetry between ENA and the western Mediterranean (EU) is similar to land-ocean climatic proxies (Sánchez Goñi et al., 2002).

The pollen records from the East Asian Islands (Taiwan and Japan) and northeast China show no biome change but millennial-scale pollen percentage variability associated with DO cycles indicating warmer and wetter conditions during Greenland Interstadials (Mingram et al., 2018; Takahara et al., 2010). Those studies have interpreted the vegetation changes as strengthening of the Asian summer monsoon, consistent with our simulation (EA in Figs. S10 and S13). Moreover, pollen-inferred vegetation changes using a marine record from the Bay of Bengal also show the millennial-scale variability between woody-savanna mosaics and grasslands associated with DO cycles showing wetter during Greenland interstadials (Zorzi et al., 2022), and our simulation shows vegetation shifts from bare soil to C4 grasses associated with strengthening of the Indian summer monsoon during GIs (IN Figs. S11 and S14).

The vegetation distribution in the circum-Atlantic tropics in Africa and South America is strongly coupled to the ITCZ location. Thus, the pollen records from the northern and southern limits of the ITCZ in South America show vegetation responses to DO cycles (Harrison and Sánchez Goñi, 2010; Hessler et al., 2010). In contrast, several African pollen records (Lézine et al., 2019; Mulitza et al., 2008) show changes in vegetation in response to the Heinrich events, not the DO events, and the absence of response associated with DO warming is a real phenomenon in West Africa. The observed responses imply that climate changes in West Africa are associated with a southward shift of the ITCZ, and the northern limit of the ITCZ does not reach the data sites in the boreal summer. Our simulation shows that northward expansion of C4 grasses in the Sahel due to the strengthening of the summer monsoon might be a natural response in GIs (SHL in Figs. S11 and S14), but it does not show that the ITCZ shifts sufficiently southward in GSs.

The pollen records from tropical South America show a strong response of vegetation to DO cycles (González et al., 2008; Hessler et al., 2010). The higher pollen concentration and the extension of forests happened during interstadial periods in the northern sites of the ITCZ, while the opposite response was shown in the southern sites of the ITCZ, suggesting vegetation responses associated with the shift of the ITCZ. On the other hand, pollen records in southeast Brazil and western South America do not show abrupt changes that are consistently associated with DO variability. The response is not as strong as that observed in extra-tropical regions and is consistent with attenuating the North Atlantic climate signal into the tropical regions.

Vegetation changes in western and central Australia, where pollen data do not exist, are not large, but our simulation shows specific vegetation changes; bare soil replaces C3 grass and shrub during GIs because of increased precipitation. It does not show large-scale atmospheric circulation over Australia associated with millennial-scale variability (Fig. S6) but shows robust responses of both precipitation and vegetation because of biogeophysical climate feedbacks. The feedback processes may be similar to how forest cover plays an important role in increasing rainfall due to an

increase in atmospheric water vapour (Sheil and Murdiyarso, 2009).

The TRIFFID dynamic global vegetation model has only five PFTs. Therefore, vegetation changes among those PFTs can be discussed, but it is hard to identify more detailed vegetation changes, for example, among forest types such as tropical, warm-temperate, temperate, and boreal, as well as the variation between C3 grass and tundra. Thus, it is necessary to use a more complex DGVM, such as an LPJ model (Chaste et al., 2018), to discuss vegetation changes in more detail. This modelling will be the subject of future work.

5. Summary

The HadCM3B-M2.1 model with the 30 ka BP boundary condition demonstrates millennial-scale climate oscillations along the salt oscillation hypothesis. This unforced glacial simulation reproduced some of the sawtooth-shaped oscillation, characterised by rapid warming followed by progressive cooling, with a timescale of ca. 1500 years, and these features are consistent with the oxygen isotope $\delta^{18}\text{O}$ data from the NGRIP ice core. Moreover, the magnitude of the simulated temperature warming at the NGRIP is $7.1 \pm 2.5^\circ\text{C}$, equivalent to the DO6, the smallest temperature change in the observed DO events.

The simulated temperature over the Northern Hemisphere, especially in the wintertime North Atlantic and Beringia during Greenland interstadials (GIs), is warmer than Greenland stadials (GSs), and the amplitude declines as moving toward low latitudes. Moreover, the temperature changes in the Southern Hemisphere are very small and not robust. The simulated precipitation during GIs is also higher than GSs, which correlates with the temperature. Rates of precipitation changes in the Northern Hemisphere extratropics (NHEXT) are similar to one in the Northern Hemisphere tropics (NTROP), while temperature changes in the NHEXT are larger than in the NTROP. Therefore, the precipitation changes in NTROP are expected to result from changes in dynamics factors rather than thermodynamic factors. Compared to GSs, the simulated boreal summer precipitation during GIs increases over the Northern Hemisphere tropics and monsoon regions such as the Indian subcontinent and West Africa due to the ITCZ northward migration and strengthening of the boreal summer monsoon. The simulated austral summer precipitation also increases in some regions of the Southern Hemisphere, such as the Amazon, South Africa, and Australia. The simulated precipitation changes between eastern North America and Europe are opposite, a present-day negative mode of NAO-like configuration.

The global and annual mean ITCZ location moves northward in GIs and southward in GSs by $0.8^\circ \pm 0.6^\circ$ except for the western tropical Pacific and the eastern Indian Ocean. The monsoon indices with the simulated 850 hPa westerlies show that the Indian monsoon strengthens, but both the East Asian monsoon and South American monsoon weaken in GIs relative to GSs. On the other hand, the Australian summer monsoon does not show a strong relationship with the millennial-scale climate variability in Greenland.

TRIFFID dynamic vegetation model simulates the PFT changes associated with the DO-like millennial-scale climate variability, but the amplitude is small, and the dominant PFT changes happen in limited areas such as the interior of Eurasia. In the Northern Hemisphere extratropics, the shrubs and needleleaf trees increase, while C3 grasses decrease during GIs. C4 grasses and broadleaf trees in the Northern Hemisphere tropics increase during GIs. Thus, the fractional coverage of bare soil decreases during GIs relative to GSs. The PFT's response time to climate changes is several years to decades for shrubs and grasses and several hundred years for trees. Thus, the peak times of expansion/shrinkage of tree PFTs are

Table 3

data-model comparison about the climate responses in Greenland interstadials relative to Greenland stadials.

Region or system	Observed response(s)	Simulated response(s)
Greenland	Abrupt-large warming	Less abrupt-large warming
Central Europe	Warmer and wetter	Warmer and wetter
Western Europe	Warmer and wetter	Warmer and wetter
Eastern Mediterranean	Warmer and wetter	Warmer
East Central Siberia	Warmer	Warmer
The Great Basin	Warmer and wetter	Warmer
Southwestern USA	Warmer and drier	Warmer and wetter
The Pacific Northwest	Warmer	Warmer and wetter
The Florida Peninsula	Drier	Drier
North African monsoon	Stronger summer monsoon	Stronger summer monsoon
East Asian monsoon	Stronger summer monsoon	Weaker summer monsoon
Indian monsoon	Stronger summer monsoon	Stronger summer monsoon
Central America/Tropical North Atlantic	Wetter in tropical Americas, ITCZ northward	Wetter in tropical Americas, ITCZ northward
South American summer monsoon	Weaker summer monsoon	Weaker summer monsoon
South African monsoon	Weaker summer monsoon	Wetter
subtropical Australia	ITCZ equatorward	No specific ITCZ migration
NW tropical Pacific	Lower salinity	Higher salinity
NE Australia	Drier	No robust change
Antarctica	Gradual-small cooling	Gradual-small cooling

displaced later than GIs and GSs. Millennial-scale PFTs' variability is also shown in the Southern Hemisphere tropics, but their phases are out of phase with that of the Northern Hemisphere. In GIs, the simulated needleleaf trees increase in south Europe, the C3 grasses increase in central Asia and western-southern Australia and decrease in Europe, shrubs increase in the interior of Eurasia, and C4 grasses increase in West Africa, the Indian subcontinent, and northeastern South America.

Our simulation successfully represents lots of the observed responses associated with DO-like warming, especially temperature increases in the Northern Hemisphere and hydroclimate changes in the tropics, such as strengthening the Northern Hemisphere summer monsoon and the northward shift of the ITCZ (Table 3). Moreover, an observed teleconnection pattern of precipitation between south-eastern North America and southern Europe is sufficiently simulated. On the other hand, the simulated East Asian and South African monsoons and climate variations in the western Pacific and northern Australia are inconsistent with observed responses. The simulated precipitation changes in the Northern Hemisphere extratropics, especially in North America, are also not well represented despite a teleconnection of wintertime precipitation between western and south-eastern North America.

The HadCM3B-M2.1 model simulation based on the salt oscillation hypothesis represents Dansgaard-Oeschger (DO)-like millennial-scale climate variability in a glacial state. It captures lots of the observed large-scale climate variations in and beyond the North Atlantic but some mismatches, especially in the equatorial Indian Ocean and the western Pacific Ocean. To better understand DO cycles, it is necessary to further examine whether the causes of those data-model mismatches are dependent on the salt oscillation hypothesis or the climate model.

Credit author statement

K.I and P.J.V designed this study, and P.J.V. carried out the simulation. K.I performed the analysis. K.I prepared the first draft of the paper, and all authors modify the manuscript.

Declaration of competing interest

The authors declare that they have no known competing financial interests or personal relationships that could have appeared to influence the work reported in this paper.

Data availability

The output from model simulation is available from <https://www.paleo.bristol.ac.uk/ummodel/scripts/papers>.

Acknowledgements

This work was carried out using the computational facilities of the Advanced Computing Research Centre, University of Bristol—<http://www.bris.ac.uk/acrc> (Bluecrystal). This work was also supported by the TiPES project in the European Union Horizon 2020 program (grant no. 820970) and the Natural Environment Research Council (NERC) in the United Kingdom (NE/S001743/1). This is TiPES contribution no. 219. We thank you two anonymous reviewers and editor for the constructive comments and suggestions, which have helped to improve the manuscript.

Appendix A. Supplementary data

Supplementary data to this article can be found online at <https://doi.org/10.1016/j.quascirev.2023.108016>.

References

- Adolphi, F., Bronk Ramsey, C., Erhardt, T., Edwards, R.L., Cheng, H., Turney, C.S.M., Cooper, A., Svensson, A., Rasmussen, S.O., Fischer, H., Muscheler, R., 2018. Connecting the Greenland ice-core and U/Th timescales via cosmogenic radionuclides: testing the synchronicity of Dansgaard-Oeschger events. *Clim. Past* 14, 1755–1781.
- Andersen, K.K., Azuma, N., Barnola, J.M., Bigler, M., Biscaye, P., Caillon, N., Chappellaz, J., Clausen, H.B., Dahl-Jensen, D., Fischer, H., Flückiger, J., Fritzsch, D., Fujii, Y., Goto-Azuma, K., Grönvold, K., Gundestrup, N.S., Hansson, M., Huber, C., Hvidberg, C.S., Johnsen, S.J., Jonsell, U., Jouzel, J., Kipfstuhl, S., Landais, A., Leuenberger, M., Lorrain, R., Masson-Delmotte, V., Miller, H., Motoyama, H., Narita, H., Popp, T., Rasmussen, S.O., Raynaud, D., Rothlisberger, R., Ruth, U., Samyn, D., Schwander, J., Shoji, H., Siggard-Andersen, M.L., Steffensen, J.P., Stocker, T., Sveinbjörnsdóttir, A.E., Svensson, A., Takata, M., Tison, J.L., Thorsteinsson, T., Watanabe, O., Wilhelms, F., White, J.W.C., North Greenland Ice Core Project, m., 2004. High-resolution record of Northern Hemisphere climate extending into the last interglacial period. *Nature* 431, 147–151.
- Armstrong, E., Hopcroft, P.O., Valdes, P.J., 2019. A simulated Northern Hemisphere terrestrial climate dataset for the past 60,000 years. *Sci. Data* 6, 265.
- Armstrong, E., Izumi, K., Valdes, P., 2022. Identifying the mechanisms of DO-scale oscillations in a GCM: a salt oscillator triggered by the Laurentide ice sheet. *Clim. Dynam.* <https://doi.org/10.1007/s00382-022-06564-y>.
- Armstrong, E., Valdes, P., House, J., Singarayer, J., 2017. Investigating the impact of CO₂ on low-frequency variability of the AMOC in HadCM3. *J. Clim.* 30, 7863–7883.
- Asmerom, Y., Polyak, V.J., Burns, S.J., 2010. Variable winter moisture in the

- southwestern United States linked to rapid glacial climate shifts. *Nat. Geosci.* 3, 114–117.
- Barker, S., Knorr, G., Edwards, R.L., Parrenin, F., Putnam, A.E., Skinner, L.C., Wolff, E., Ziegler, M., 2011. 800,000 Years of abrupt climate variability. *Science* 334, 347–351.
- Bayon, G., De Deckker, P., Magee, J.W., Germain, Y., Bermell, S., Tachikawa, K., Norman, M.D., 2017. Extensive wet episodes in Late Glacial Australia resulting from high-latitude forcings. *Sci. Rep.* 7, 44054.
- Benson, L., Lund, S., Negrini, R., Linsley, B., Zic, M., 2003. Response of North American great basin lakes to Dansgaard-Oeschger oscillations. *Quat. Sci. Rev.* 22, 2239–2251.
- Berger, A., Loutre, M.F., Gallée, H., 1998. Sensitivity of the LLN climate model to the astronomical and CO₂ forcings over the last 200 ky. *Clim. Dynam.* 14, 615–629.
- Blunier, T., Chappellaz, J., Schwander, J., Dällenbach, A., Stauffer, B., Stocker, T.F., Raynaud, D., Jouzel, J., Clausen, H.B., Hammer, C.U., Johnsen, S.J., 1998. Asynchrony of Antarctic and Greenland climate change during the last glacial period. *Nature* 394, 739–743.
- Bond, G., Broecker, W., Johnsen, S., McManus, J., Labeyrie, L., Jouzel, J., Bonani, G., 1993. Correlations between climate records from North Atlantic sediments and Greenland ice. *Nature* 365, 143–147.
- Bond, G., Heinrich, H., Broecker, W., Labeyrie, L., McManus, J., Andrews, J., Huon, S., Jantschik, R., Clasen, S., Simet, C., Tedesco, K., Klas, M., Bonani, G., Ivy, S., 1992. Evidence for massive discharges of icebergs into the North Atlantic ocean during the last glacial period. *Nature* 360, 245–249.
- Buizert, C., Adrian, B., Ahn, J., Albert, M., Alley, R.B., Baggenstos, D., Bauska, T.K., Bay, R.C., Bencivengo, B.B., Bentley, C.R., Brook, E.J., Chellman, N.J., Clow, G.D., Cole-Dai, J., Conway, H., Cravens, E., Cuffey, K.M., Dunbar, N.W., Edwards, J.S., Fegyveresi, J.M., Ferris, D.G., Fitzpatrick, J.J., Fudge, T.J., Gibson, C.J., Gkinis, V., Goetz, J.J., Gregory, S., Hargreaves, G.M., Iverson, N., Johnson, J.A., Jones, T.R., Kalk, M.L., Kippenhan, M.J., Koffman, B.G., Kreutz, K., Kuhl, T.W., Lebar, D.A., Lee, J.E., Marcott, S.A., Markle, B.R., Maselli, O.J., McConnell, J.R., McGwire, K.C., Mitchell, L.E., Mortensen, N.B., Neff, P.D., Nishiizumi, K., Nunn, R.M., Orsi, A.J., Pasteris, D.R., Pedro, J.B., Pettit, E.C., Buford Price, P., Priscu, J.C., Rhodes, R.H., Rosen, J.L., Schauer, A.J., Schoenemann, S.W., Sendelbach, P.J., Severinghaus, J.P., Shturmakov, A.J., Sigl, M., Slawny, K.R., Souney, J.M., Sowers, T.A., Spencer, M.K., Steig, E.J., Taylor, K.C., Twickler, M.S., Vaughn, B.H., Voigt, D.E., Waddington, E.J., Welten, K.C., Wendricks, A.W., White, J.W.C., Winstrup, M., Wong, G.J., Woodruff, T.E., Members, W.D.P., 2015. Precise interglacial phasing of abrupt climate change during the last ice age. *Nature* 520, 661–665.
- Carolin, S.A., Cobb, K.M., Adkins, J.F., Clark, B., Conroy, J.L., Lejau, S., Malang, J., Tuen, A.A., 2013. Varied response of western Pacific hydrology to climate forcings over the last glacial period. *Science* 340, 1564–1566.
- Case, T., 2000. *An Illustrated Guide to Theoretical Ecology*. Oxford University Press, Oxford, UK.
- Chaste, E., Girardin, M.P., Kaplan, J.O., Portier, J., Bergeron, Y., Hély, C., 2018. The pyrogeography of eastern boreal Canada from 1901 to 2012 simulated with the LPJ-LMfire model. *Biogeosciences* 15, 1273–1292.
- Cheng, H., Sinha, A., Cruz, F.W., Wang, X., Edwards, R.L., d'Horta, F.M., Ribas, C.C., Vuille, M., Stott, L.D., Auler, A.S., 2013. Climate change patterns in Amazonia and biodiversity. *Nat. Commun.* 4, 1411.
- Cheng, H., Sinha, A., Wang, X., Cruz, F.W., Edwards, R.L., 2012. The global paleomonsoon as seen through speleothem records from Asia and the Americas. *Clim. Dynam.* 39, 1045–1062.
- Chiang, J.C.H., Bitz, C.M., 2005. Influence of high latitude ice cover on the marine Intertropical Convergence Zone. *Clim. Dynam.* 25, 477–496.
- Clement, A.C., Peterson, L.C., 2008. Mechanisms of abrupt climate change of the last glacial period. *Rev. Geophys.* 46.
- Corrick, E.C., Drysdale, R.N., Hellstrom, J.C., Capron, E., Rasmussen, S.O., Zhang, X., Fleitmann, D., Couchoud, I., Wolff, E., 2020. Synchronous timing of abrupt climate changes during the last glacial period. *Science* 369, 963–969.
- Cox, P.M., 2001. In: Office, M. (Ed.), *Description of the "TRIFFID" Dynamic Global Vegetation Model*.
- Cox, P.M., Betts, R.A., Jones, C.D., Spall, S.A., Totterdell, I.J., 2000. Acceleration of global warming due to carbon-cycle feedbacks in a coupled climate model. *Nature* 408, 184–187.
- Cox, P.M., Huntingford, C., Harding, R.J., 1998. A canopy conductance and photosynthesis model for use in a GCM land surface scheme. *J. Hydrol.* 212–213, 79–94.
- Dansgaard, W., Johnsen, S.J., Clausen, H.B., Dahl-Jensen, D., Gundestrup, N.S., Hammer, C.U., Hvidberg, C.S., Steffensen, J.P., Sveinbjörnsdóttir, A.E., Jouzel, J., Bond, G., 1993. Evidence for general instability of past climate from a 250-kyr ice-core record. *Nature* 364, 218–220.
- Davies-Barnard, T., Ridgwell, A., Singarayer, J., Valdes, P., 2017. Quantifying the influence of the terrestrial biosphere on glacial–interglacial climate dynamics. *Clim. Past* 13, 1381–1401.
- Denniston, R.F., Asmerom, Y., Polyak, V., Dorale, J.A., Carpenter, S.J., Trodick, C., Hoyer, B., González, L.A., 2007. Synchronous millennial-scale climatic changes in the Great Basin and the North Atlantic during the last interglacial. *Geology* 35, 619–622.
- Deplazes, G., Lückge, A., Peterson, L.C., Timmermann, A., Hamann, Y., Hughen, K.A., Röhl, U., Laj, C., Cane, M.A., Sigman, D.M., Haug, G.H., 2013. Links between tropical rainfall and North Atlantic climate during the last glacial period. *Nat. Geosci.* 6, 213–217.
- Deplazes, G., Lückge, A., Stuut, J.-B.W., Pätzold, J., Kuhlmann, H., Husson, D., Fant, M., Haug, G.H., 2014. Weakening and strengthening of the Indian monsoon during Heinrich events and Dansgaard-Oeschger oscillations. *Paleoceanography* 29, 99–114.
- Ditlevsen, P.D., Andersen, K.K., Svensson, A., 2007. The DO-climate events are probably noise induced: statistical investigation of the claimed 1470 years cycle. *Clim. Past* 3, 129–134.
- Donders, T.H., de Boer, H.J., Finsinger, W., Grimm, E.C., Dekker, S.C., Reichert, G.J., Wagner-Cremer, F., 2011. Impact of the Atlantic warm pool on precipitation and temperature in Florida during North Atlantic cold spells. *Clim. Dynam.* 36, 109–118.
- Dong, J., Shen, C.-c., Kong, X., Wang, Y., Duan, F., 2018. Asian monsoon dynamics at Dansgaard/Oeschger events 1T 8 and Heinrich events U 4 in northern China. *Quat. Geochronol.* 47, 72–80.
- Donohoe, A., Marshall, J., Ferreira, D., Mcgee, D., 2013. The relationship between ITCZ location and cross-equatorial atmospheric heat transport: from the seasonal cycle to the last glacial maximum. *J. Clim.* 26, 3597–3618.
- Duan, F., Liu, D., Cheng, H., Wang, X., Wang, Y., Kong, X., Chen, S., 2014. A high-resolution monsoon record of millennial-scale oscillations during Late MIS 3 from Wulu Cave, south-west China. *J. Quat. Sci.* 29, 83–90.
- Essery, R., Best, M., Cox, P.M., 2001. In: Office, M. (Ed.), *MOSES 2.2 Technical Documentation*.
- Fleitmann, D., Cheng, H., Badertscher, S., Edwards, R.L., Mudelsee, M., Gökürk, O.M., Fankhauser, A., Pickering, R., Raible, C.C., Matter, A., Kramers, J., Tüysüz, O., 2009. Timing and climatic impact of Greenland interstadials recorded in stalagmites from northern Turkey. *Geophys. Res. Lett.* 36.
- Fletcher, W.J., Sánchez Goni, M.F., 2008. Orbital- and sub-orbital-scale climate impacts on vegetation of the western Mediterranean basin over the last 48,000 yr. *Quat. Res.* 70, 451–464.
- Fletcher, W.J., Sánchez Goni, M.F., Allen, J.R.M., Cheddadi, R., Combourieu-Nebout, N., Huntley, B., Lawson, I., Londeix, L., Magri, D., Margari, V., Müller, U.C., Naughton, F., Novenko, E., Roucoux, X., Tzedakis, P.C., 2010. Millennial-scale variability during the last glacial in vegetation records from Europe. *Quat. Sci. Rev.* 29, 2839–2864.
- Frierson, D.M.W., Hwang, Y.-T., 2012. Extratropical influence on ITCZ shifts in slab ocean simulations of global warming. *J. Clim.* 25, 720–733.
- Gadgil, S., 2018. The monsoon system: land–sea breeze or the ITCZ? *J. Earth Syst. Sci.* 127, 1.
- Gan, M.A., Rao, V.B., Moscati, M.C.L., 2005. South American monsoon indices. *Atmos. Sci. Lett.* 6, 219–223.
- Ganopolski, A., Rahmstorf, S., 2001. Rapid changes of glacial climate simulated in a coupled climate model. *Nature* 409, 153–158.
- Genty, D., Combourieu Nebout, N., Hatté, C., Blamart, D., Ghaleb, B., Isabelle, L., 2005. Rapid climatic changes of the last 90 kyr recorded on the European continent. *Compt. Rendus Geosci.* 337, 970–982.
- González, C., Dupont, L.M., Behling, H., Wefer, G., 2008. Neotropical vegetation response to rapid climate changes during the last glacial period: palynological evidence from the Cariaco Basin. *Quat. Res.* 69, 217–230.
- Gordon, C., Cooper, C., Senior, C.A., Banks, H., Gregory, J.M., Johns, T.C., Mitchell, J.F.B., Wood, R.A., 2000. The simulation of SST, sea ice extents and ocean heat transports in a version of the Hadley Centre coupled model without flux adjustments. *Clim. Dynam.* 16, 147–168.
- Grigg, L.D., Whitlock, C., 2002. Patterns and causes of millennial-scale climate change in the Pacific Northwest during Marine Isotope Stages 2 and 3. *Quaternary Science Reviews* 21, 2067–2083.
- Grimm, E.C., Watts, W.A., Jacobson, G.L., Hansen, B.C.S., Almquist, H., Dieffenbacher-Krall, A.C., 2006. Evidence for warm wet Heinrich events in Florida. *Quat. Sci. Rev.* 25, 2197–2211.
- Grygar, T., Kadlec, J., Pruner, P., Swann, G., Bezdička, P., Hradil, D., Lang, K., Novotná, K., Oberhänsli, H., 2006. Paleoenvironmental record in Lake Baikal sediments: environmental changes in the last 160 ky. *Palaeogeogr. Palaeoclimatol. Palaeoecol.* 237, 240–254.
- Harrison, S.P., Sánchez Goni, M.F., 2010. Global patterns of vegetation response to millennial-scale variability and rapid climate change during the last glacial period. *Quat. Sci. Rev.* 29, 2957–2980.
- Hemming, S.R., 2004. Heinrich events: massive late Pleistocene detritus layers of the North Atlantic and their global climate imprint. *Rev. Geophys.* 42.
- Henry, L.G., McManus, J.F., Curry, W.B., Roberts, N.L., Piotrowski, A.M., Keigwin, L.D., 2016. North Atlantic ocean circulation and abrupt climate change during the last glaciation. *Science* 353, 470–474.
- Hessler, I., Dupont, L., Bonnefille, R., Behling, H., González, C., Helmens, K.F., Hooghiemstra, H., Lebamba, J., Ledru, M.-P., Lézine, A.-M., Maley, J., Marret, F., Vincens, A., 2010. Millennial-scale changes in vegetation records from tropical Africa and South America during the last glacial. *Quat. Sci. Rev.* 29, 2882–2899.
- Hughes, J.K., 2003. The dynamic response of the global atmosphere–vegetation coupled system. In: *Department of Meteorology. The University of Reading*.
- Jensen, M.F., Nummelin, A., Nielsen, S.B., Sadatzki, H., Sessford, E., Risebrobakken, B., Andersson, C., Voelker, A., Roberts, W.H.G., Pedro, J., Born, A., 2018. A spatiotemporal reconstruction of sea-surface temperatures in the North Atlantic during Dansgaard–Oeschger events 5–8. *Clim. Past* 14, 901–922.
- Jiménez-Moreno, G., Anderson, R.S., Desprat, S., Grigg, L.D., Grimm, E.C., Heusser, L.E., Jacobs, B.F., López-Martínez, C., Whitlock, C.L., Willard, D.A., 2010. Millennial-scale variability during the last glacial in vegetation records from North America. *Quat. Sci. Rev.* 29, 2865–2881.
- Kajikawa, Y., Wang, B., Yang, J., 2010. A multi-time scale Australian monsoon index. *Int. J. Climatol.* 30, 1114–1120.
- Kanner, L.C., Burns, S.J., Cheng, H., Edwards, R.L., 2012. High-latitude forcing of the

- South American summer monsoon during the last glacial. *Science* 335, 570–573.
- Kaplan, J.O., Bigelow, N.H., Prentice, I.C., Harrison, S.P., Bartlein, P.J., Christensen, T.R., Cramer, W., Matveyeva, N.V., McGuire, A.D., Murray, D.F., Razzhivin, V.Y., Smith, B., Walker, D.A., Anderson, P.M., Andreev, A.A., Brubaker, L.B., Edwards, M.E., Lozhkin, A.V., 2003. Climate change and Arctic ecosystems: 2. Modeling, paleodata-model comparisons, and future projections. *J. Geophys. Res. Atmos.* 108.
- Kathayat, G., Cheng, H., Sinha, A., Spötl, C., Edwards, R.L., Zhang, H., Li, X., Yi, L., Ning, Y., Cai, Y., Lui, W.L., Breitenbach, S.F.M., 2016. Indian monsoon variability on millennial-orbital timescales. *Sci. Rep.* 6, 24374.
- Kindler, P., Guillemin, M., Baumgartner, M., Schwander, J., Landais, A., Leuenberger, M., 2014. Temperature reconstruction from 10 to 120 kyr b2k from the NGRIP ice core. *Clim. Past* 10, 887–902.
- Klockmann, M., Mikolajewicz, U., Kleppin, H., Marotzke, J., 2020. Coupling of the subpolar gyre and the overturning circulation during abrupt glacial climate transitions. *Geophys. Res. Lett.* 47, e2020GL090361.
- Knutti, R., Flückiger, J., Stocker, T.F., Timmermann, A., 2004. Strong hemispheric coupling of glacial climate through freshwater discharge and ocean circulation. *Nature* 430, 851–856.
- Kuniyoshi, Y., Abe-Ouchi, A., Sheriff-Tadano, S., Chan, W.-L., Saito, F., 2022. Effect of climatic precession on Dansgaard-Oeschger-like oscillations. *Geophys. Res. Lett.* 49, e2021GL095695.
- Lauterbach, S., Andersen, N., Wang, Y.V., Blanz, T., Larsen, T., Schneider, R.R., 2020. An ~130 kyr record of surface water temperature and $\delta^{18}\text{O}$ from the northern Bay of Bengal: investigating the linkage between Heinrich events and weak monsoon intervals in Asia. *Paleoceanogr. Paleoclimatol.* 35, e2019PA003646.
- Leduc, G., Vidal, L., Tachikawa, K., Rostek, F., Sonzogni, C., Beaufort, L., Bard, E., 2007. Moisture transport across Central America as a positive feedback on abrupt climatic changes. *Nature* 445, 908–911.
- Lézine, A.-M., Izumi, K., Kageyama, M., Achoundong, G., 2019. A 90,000-year record of Afromontane forest responses to climate change. *Science* 363, 177–181.
- Li, C., Born, A., 2019. Coupled atmosphere-ice-ocean dynamics in Dansgaard-Oeschger events. *Quat. Sci. Rev.* 203, 1–20.
- Loulergue, L., Schilt, A., Spahni, R., Masson-Delmotte, V., Blunier, T., Lemieux, B., Barnola, J.-M., Raynaud, D., Stocker, T.F., Chappellaz, J., 2008. Orbital and millennial-scale features of atmospheric CH_4 over the past 800,000 years. *Nature* 453, 383–386.
- Masson-Delmotte, V., Jouzel, J., Landais, A., Stievenard, M., Johnsen, S.J., White, J.W.C., Werner, M., Sveinbjornsdottir, A., Fuhrer, K., 2005. GRIP deuterium excess reveals rapid and orbital-scale changes in Greenland moisture origin. *Science* 309, 118–121.
- Medina-Elizalde, M., Burns, S.J., Polanco-Martinez, J., Lasen-Hernández, F., Bradley, R., Wang, H.-C., Shen, C.-C., 2017. Synchronous precipitation reduction in the American Tropics associated with Heinrich 2. *Sci. Rep.* 7, 11216.
- Mingram, J., Stebich, M., Schettler, G., Hu, Y., Rioual, P., Nowaczyk, N., Dulski, P., You, H., Opitz, S., Liu, Q., Liu, J., 2018. Millennial-scale East Asian monsoon variability of the last glacial deduced from annually laminated sediments from Lake Sihailongwan, N.E. China. *Quat. Sci. Rev.* 201, 57–76.
- Mosblech, N.A.S., Bush, M.B., Gosling, W.D., Hodel, D., Thomas, L., van Calsteren, P., Correa-Metrio, A., Valencia, B.G., Curtis, J., van Woesik, R., 2012. North Atlantic forcing of Amazonian precipitation during the last ice age. *Nat. Geosci.* 5, 817–820.
- Moseley, G.E., Spötl, C., Svensson, A., Cheng, H., Brandstätter, S., Edwards, R.L., 2014. Multi-speleothem record reveals tightly coupled climate between central Europe and Greenland during Marine Isotope Stage 3. *Geology* 42, 1043–1046.
- Mulitza, S., Prange, M., Stuut, J.-B., Zabel, M., von Döbenek, T., Itambi, A.C., Nizou, J., Schulz, M., Wefer, G., 2008. Sahel megadroughts triggered by glacial slowdowns of Atlantic meridional overturning. *Paleoceanography* 23.
- Nebout, N.C., Turon, J.L., Zahn, R., Capotondi, L., Londeix, L., Pahnke, K., 2002. Enhanced aridity and atmospheric high-pressure stability over the western Mediterranean during the North Atlantic cold events of the past 50 k. y. *Geology* 30, 863–866.
- Overpeck, J.T., Cole, J.E., 2006. Abrupt change in earth's climate system. *Annu. Rev. Environ. Resour.* 31, 1–31.
- Partin, J.W., Cobb, K.M., Adkins, J.F., Clark, B., Fernandez, D.P., 2007. Millennial-scale trends in west Pacific warm pool hydrology since the Last Glacial Maximum. *Nature* 449, 452–455.
- Pedro, J.B., Andersson, C., Vettoretti, G., Voelker, A.H.L., Waelbroeck, C., Dokken, T.M., Jensen, M.F., Rasmussen, S.O., Sessford, E.G., Jochum, M., Nisanoglu, K.H., 2022. Dansgaard-Oeschger and Heinrich event temperature anomalies in the North Atlantic set by sea ice, frontal position and thermocline structure. *Quat. Sci. Rev.* 289, 107599.
- Peltier, W.R., 2004. Global glacial isostasy and the surface of the ice-age earth: the ICE-5G (VM2) model and grace. *Annu. Rev. Earth Planet Sci.* 32, 111–149.
- Peltier, W.R., Ma, Y., Chandan, D., 2020. The KPP trigger of rapid AMOC intensification in the nonlinear dansgaard-oeschger relaxation oscillation. *J. Geophys. Res.: Oceans* 125, e2019JC015557.
- Peltier, W.R., Vettoretti, G., 2014. Dansgaard-Oeschger oscillations predicted in a comprehensive model of glacial climate: a “kicked” salt oscillator in the Atlantic. *Geophys. Res. Lett.* 41, 7306–7313.
- Petersen, S.V., Schrag, D.P., Clark, P.U., 2013. A new mechanism for Dansgaard-Oeschger cycles. *Paleoceanography* 28, 24–30.
- Peterson, L.C., Haug, G.H., Hughen, K.A., Röhl, U., 2000. Rapid changes in the hydrologic cycle of the tropical Atlantic during the last glacial. *Science* 290, 1947–1951.
- Petit, J.R., Jouzel, J., Raynaud, D., Barkov, N.I., Barnola, J.M., Basile, I., Bender, M., Chappellaz, J., Davis, M., Delaygue, G., Delmotte, M., Kotlyakov, V.M., Legrand, M., Lipenkov, V.Y., Lorius, C., Pépin, L., Ritz, C., Saltzman, E., Stievenard, M., 1999. Climate and atmospheric history of the past 420,000 years from the Vostok ice core, Antarctica. *Nature* 399, 429–436.
- Piotrowski, A.M., Goldstein, S.L., Hemming, S.R., Fairbanks, R.G., Zylberberg, D.R., 2008. Oscillating glacial northern and southern deep water formation from combined neodymium and carbon isotopes. *Earth Planet Sci. Lett.* 272, 394–405.
- Pisias, N.G., Clark, P.U., Brook, E.J., 2010. Modes of global climate variability during marine isotope stage 3 (60–26 ka). *J. Clim.* 23, 1581–1588.
- Roucoux, K.H., de Abreu, L., Shackleton, N.J., Tzedakis, P.C., 2005. The response of NW Iberian vegetation to North Atlantic climate oscillations during the last 65 kyr. *Quat. Sci. Rev.* 24, 1637–1653.
- Roucoux, K.H., Shackleton, N.J., de Abreu, L., Schönfeld, J., Tzedakis, P.C., 2001. Combined marine proxy and pollen analyses reveal rapid Iberian vegetation response to North Atlantic millennial-scale climate oscillations. *Quat. Res.* 56, 128–132.
- Rousseau, D.-D., Sima, A., Antoine, P., Hatté, C., Lang, A., Zöller, L., 2007. Link between European and North Atlantic abrupt climate changes over the last glaciation. *Geophys. Res. Lett.* 34.
- Sadatzi, H., Dokken, T.M., Berben, S.M.P., Muschitiello, F., Stein, R., Fahl, K., Menviel, L., Timmermann, A., Jansen, E., 2019. Sea ice variability in the southern Norwegian Sea during glacial Dansgaard-Oeschger climate cycles. *Sci. Adv.* 5, eaau6174.
- Sadatzi, H., Maffezzoli, N., Dokken, T.M., Simon, M.H., Berben, S.M.P., Fahl, K., Kjær, H.A., Spolaor, A., Stein, R., Vallelonga, P., Vinther, B.M., Jansen, E., 2020. Rapid reductions and millennial-scale variability in Nordic Seas sea ice cover during abrupt glacial climate changes. *Proc. Natl. Acad. Sci. USA* 117, 29478–29486.
- Sánchez Goñi, M., Cacho, I., Turon, J., Guiot, J., Sierro, F., Peyrouquet, J., Grimalt, J., Shackleton, N., 2002. Synchronicity between marine and terrestrial responses to millennial scale climatic variability during the last glacial period in the Mediterranean region. *Clim. Dynam.* 19, 95–105.
- Sánchez Goñi, M.A.F., Turon, J.-L., Eynaud, F., Gendreau, S., 2000. European climatic response to millennial-scale changes in the atmosphere-ocean system during the last glacial period. *Quat. Res.* 54, 394–403.
- Sánchez Goñi, M.F., Landais, A., Fletcher, W.J., Naughton, F., Desprat, S., Duprat, J., 2008. Contrasting impacts of Dansgaard-Oeschger events over a western European latitudinal transect modulated by orbital parameters. *Quat. Sci. Rev.* 27, 1136–1151.
- Schulz, H., von Rad, U., Erlenkeuser, H., von Rad, U., 1998. Correlation between Arabian Sea and Greenland climate oscillations of the past 110,000 years. *Nature* 393, 54–57.
- Schulz, M., 2002. On the 1470-year pacing of Dansgaard-Oeschger warm events. *Paleoceanography* 17, 4-1-4-9.
- Sheil, D., Murdiyarso, D., 2009. How forests attract rain: an examination of a new hypothesis. *Bioscience* 59, 341–347.
- Singarayer, J.S., Valdes, P.J., 2010. High-latitude climate sensitivity to ice-sheet forcing over the last 120 kyr. *Quat. Sci. Rev.* 29, 43–55.
- Singarayer, J.S., Valdes, P.J., Roberts, W.H.G., 2017. Ocean dominated expansion and contraction of the late Quaternary tropical rainbelt. *Sci. Rep.* 7, 9382.
- Sinopoli, G., Masi, A., Regattieri, E., Wagner, B., Francke, A., Peyron, O., Sadori, L., 2018. Palynology of the last interglacial complex at lake Ohrid: palaeoenvironmental and palaeoclimatic inferences. *Quat. Sci. Rev.* 180, 177–192.
- Sinopoli, G., Peyron, O., Masi, A., Holtvoeth, J., Francke, A., Wagner, B., Sadori, L., 2019. Pollen-based temperature and precipitation changes in the Ohrid Basin (western Balkans) between 160 and 70 ka. *Clim. Past* 15, 53–71.
- Spahni, R., Chappellaz, J., Stocker, T.F., Loulergue, L., Hausamann, G., Kawamura, K., Flückiger, J., Schwander, J., Raynaud, D., Masson-Delmotte, V., Jouzel, J., 2005. Atmospheric methane and nitrous oxide of the late pleistocene from antarctic ice cores. *Science* 310, 1317–1321.
- Stenni, B., Masson-Delmotte, V., Selmo, E., Oerter, H., Meyer, H., Röthlisberger, R., Jouzel, J., Cattani, O., Falourd, S., Fischer, H., Hoffmann, G., Iacumin, P., Johnsen, S.J., Minster, B., Udisti, R., 2010. The deuterium excess records of EPICA Dome C and Dronning Maud Land ice cores (East Antarctica). *Quat. Sci. Rev.* 29, 146–159.
- Stocker, T.F., Johnsen, S.J., 2003. A minimum thermodynamic model for the bipolar seesaw. *Paleoceanography* 18.
- Stockhecke, M., Timmermann, A., Kipfer, R., Haug, G.H., Kwiczen, O., Friedrich, T., Menviel, L., Litt, T., Pickarski, N., Anselmetti, F.S., 2016. Millennial to orbital-scale variations of drought intensity in the Eastern Mediterranean. *Quat. Sci. Rev.* 133, 77–95.
- Stott, L., Poulsen, C., Lund, S., Thunell, R., 2002. Super ENSO and Global Climate Oscillations at Millennial Time Scales. *Science* 297, 222–226.
- Takahara, H., Igarashi, Y., Hayashi, R., Kumon, F., Liew, P.-M., Yamamoto, M., Kawai, S., Oba, T., Irino, T., 2010. Millennial-scale variability in vegetation records from the East Asian Islands: Taiwan, Japan and Sakhalin. *Quat. Sci. Rev.* 29, 2900–2917.
- Trenberth, K.E., Stepaniak, D.P., Caron, J.M., 2000. The global monsoon as seen through the divergent atmospheric circulation. *J. Clim.* 13, 3969–3993.
- Turney, C.S.M., Kershaw, A.P., Clemens, S.C., Branch, N., Moss, P.T., Keith Fifield, L.,

2004. Millennial and orbital variations of El Niño/Southern Oscillation and high-latitude climate in the last glacial period. *Nature* 428, 306–310.
- Valdes, P.J., Armstrong, E., Badger, M.P.S., Bradshaw, C.D., Bragg, F., Crucifix, M., Davies-Barnard, T., Day, J.J., Farnsworth, A., Gordon, C., Hopcroft, P.O., Kennedy, A.T., Lord, N.S., Lunt, D.J., Marzocchi, A., Parry, L.M., Pope, V., Roberts, W.H.G., Stone, E.J., Tourte, G.J.L., Williams, J.H.T., 2017. The BRIDGE HadCM3 family of climate models: HadCM3@Bristol v1.0. *Geosci. Model Dev* 10, 3715–3743.
- Vellinga, M., Wu, P., 2004. Low-latitude freshwater influence on centennial variability of the atlantic thermohaline circulation. *J. Clim.* 17, 4498–4511.
- Vettoretti, G., Peltier, W.R., 2016. Thermohaline instability and the formation of glacial North Atlantic super polynyas at the onset of Dansgaard-Oeschger warming events. *Geophys. Res. Lett.* 43, 5336–5344.
- Vettoretti, G., Peltier, W.R., 2018. Fast physics and slow physics in the nonlinear Dansgaard-Oeschger relaxation oscillation. *J. Clim.* 31, 3423–3449.
- Voelker, A.H.L., 2002. Global distribution of centennial-scale records for Marine Isotope Stage (MIS) 3: a database. *Quat. Sci. Rev.* 21, 1185–1212.
- Wagner, J.D.M., Cole, J.E., Beck, J.W., Patchett, P.J., Henderson, G.M., Barnett, H.R., 2010. Moisture variability in the southwestern United States linked to abrupt glacial climate change. *Nat. Geosci.* 3, 110–113.
- Wang, B., Ding, Q., 2008. Global monsoon: dominant mode of annual variation in the tropics. *Dynam. Atmos. Oceans* 44, 165–183.
- Wang, B., Fan, Z., 1999. Choice of south asian summer monsoon indices. *Bull. Am. Meteorol. Soc.* 80, 629–638.
- Wang, B., Wu, R., Lau, K.-M., 2001. Interannual variability of the asian summer monsoon: contrasts between the Indian and the western North Pacific? East Asian monsoons. *J. Clim.* 14, 4073–4090.
- Wang, X., Auler, A.S., Edwards, R.L., Cheng, H., Cristalli, P.S., Smart, P.L., Richards, D.A., Shen, C.-C., 2004. Wet periods in northeastern Brazil over the past 210 kyr linked to distant climate anomalies. *Nature* 432, 740–743.
- Webster, P.J., Magaña, V.O., Palmer, T.N., Shukla, J., Tomas, R.A., Yanai, M., Yasunari, T., 1998. Monsoons: processes, predictability, and the prospects for prediction. *J. Geophys. Res.: Oceans* 103, 14451–14510.
- Wei, D., González-Sampériz, P., Gil-Romera, G., Harrison, S.P., Prentice, I.C., 2021. Seasonal temperature and moisture changes in interior semi-arid Spain from the last interglacial to the Late Holocene. *Quat. Res.* 101, 143–155.
- Weldeab, 2012. Bipolar modulation of millennial-scale West African monsoon variability during the last glacial (75,000–25,000 years ago). *Quat. Sci. Rev.* 21.
- Wolff, E.W., Chappellaz, J., Blunier, T., Rasmussen, S.O., Svensson, A., 2010. Millennial-scale variability during the last glacial: the ice core record. *Quat. Sci. Rev.* 29, 2828–2838.
- Ziegler, M., Simon, M.H., Hall, I.R., Barker, S., Stringer, C., Zahn, R., 2013. Development of Middle Stone Age innovation linked to rapid climate change. *Nat. Commun.* 4, 1905.
- Zorzi, C., Desprat, S., Clément, C., Thirumalai, K., Oliviera, D., Anupama, K., Prasad, S., Martinez, P., 2022. When eastern India oscillated between desert versus savannah-dominated vegetation. *Geophys. Res. Lett.* 49, e2022GL099417.